Supplementary Information

Clark et al.
SI Text

1. Terminology

Most of these names used in this paper originated from evidence of abrupt climate changes first found in northern European floral and pollen records (1, 2) that has subsequently been identified in many other climate records elsewhere. These events are particularly well expressed in polar ice cores, where the superior resolution and chronology of these records has made them the iconic templates for defining these events (3) (Fig. 2). Other names more recently used for the Oldest Dryas interval include the "Mystery Interval" and Heinrich Stadial 1. We retain use of the Oldest Dryas in order to be consistent with its still widely used companion terminology (i.e., Bølling, Allerød, and Younger Dryas). Although this nomenclature and its variants are commonly used chronostratigraphically (4, 5), the inertia of the climate system as well as the superposition of multiple distinct regional patterns of climate change likely produced temporal differences in the global expression of the associated abrupt climate events that vary through space (6-8), providing important insights into the mechanisms responsible for them. While we thus use this terminology as a common temporal framework for discussion, establishing the spatial and temporal expression of these abrupt climate events is a particular emphasis of this paper.

2. Freshwater forcing

Modeling studies

Modeling studies consistently show that the AMOC is sensitive to the freshwater budget at the sites of deepwater formation that help drive the overturning (9). Models differ in their sensitivity to a given freshwater forcing, however, which affects all aspects of their climate response (9-13). Moreover, while the standard model experiment involves a uniform application of a freshwater flux over a given region of the ocean, the actual distribution of freshwater discharged from continental margins to the open ocean is likely much more complicated than this scenario (14, 15), introducing additional uncertainty to models typically used for paleoclimate reconstruction.

Summary of ice-sheet fluxes and routing

We derive the global ice-sheet flux from the eustatic sea-level curve shown in Figure 2E. This is the same eustatic curve from (16) except with two changes in the timing of the ice model used. First, the onset of melting at 20 ka in the former was shifted to 19.4 ka (17). Second, the melting increment starting at 19.5 ka in the former was shifted to 18.9 ka. No changes were made in the amplitudes of the melting. With the caveat that this is a eustatic curve (and not a local sea level prediction), these small changes seem to provide a slightly better fit to the time history evident in the data.

The termination of the LGM was marked by the onset of an episode of rapid sea-level rise of 5-10 m at ~19-19.5 ka (18, 19) (Fig. 2E) representing a freshwater flux of ~0.12 to 0.2 Sv (1 Sv = 10^6 m^3 s^{-1}) over 500 years (Fig. 2G) (20). An assessment of global ice-sheet history during the LGM indicates that the source of this 19-ka meltwater pulse (MWP) was the widespread retreat of Northern Hemisphere ice-sheet margins that occurred in response to insolation forcing at high northern latitudes (21).

Subsequent sea-level rise of ~15 m from ~19-14.7 ka (i.e., during the Oldest Dryas event) (Fig. 2E) can be attributed to continued retreat of the Laurentide (22, 23) and Scandinavian (24) ice sheets (Fig. 2F), representing an average freshwater flux of ~0.05 Sv to the North Atlantic during this 4.5-kyr interval (Fig. 2G). An additional freshwater flux was delivered by Heinrich event 1 at ~17 ka (Fig. 2H), but estimates of ice discharge remain highly uncertain (25).

Sea-level rise accelerated ~14.7 ka, rising 10-20 m in less than 700 years (Fig. 2E), equivalent to an average freshwater flux of 0.3 Sv over this interval (Fig. 2G). However, the source of this event, referred to as MWP-1a, remains widely debated. Its coincidence in timing with the onset of the Bølling warm interval and with a large $\delta^{18}O$ anomaly in the Gulf of Mexico led to arguments that MWP-1a was derived largely from the southern LIS (23, 26-28), but the $\delta^{18}O$ anomaly is not restricted to the time of MWP-1a, and geochemical mixing modeling of this and other similar anomalies indicates a LIS contribution of <5 m (29). There is no evidence for an acceleration in retreat of the Laurentide Ice Sheet (LIS) or Scandinavian Ice Sheet (SIS) margins at this time (22, 24) (Fig. 2F), which are the only Northern Hemisphere ice sheets with sufficient volume to account for the event. Finally, if MWP-1a were derived entirely from Northern Hemisphere ice sheets, all existing ocean models indicate that the associated freshwater flux of ~0.3 Sv over several hundred years would have caused a significant reduction of the AMOC (9, 30), which did not occur at this time (31). A substantial meltwater contribution of as much as 15 m sea-level equivalent from the Antarctic Ice Sheet (AIS), however, is supported by records indicating onset of West and East AIS retreat from its LGM position at 14.0-15.0 ka (21, 32) as well as by geophysical modeling of far-field (33, 34) and near-field (35) sea-level records.

Sea level continued to rise from ~14.0-12.9 ka at a rate and attendant freshwater flux comparable to those of the Oldest Dryas (Fig. 2E, 2G). During the Younger Dryas cold event, Northern Hemisphere ice sheets stabilized or slightly readvanced (22, 24) and rates of sea-level rise may have slowed (36, 37), raising the question as to what triggered the decrease in the AMOC (31) and associated cooling during this time. One early explanation attributed it to LIS-margin retreat that opened an eastern outlet of Lake Agassiz, routing continental runoff from the Mississippi River to the St. Lawrence River (38, 39). This hypothesis was supported by evidence for lake-level lowering and abandonment of the southern outlet (40-42) as well as by $\delta^{18}O$ records from the Gulf of Mexico that show a large salinity increase at ~12.9 ka (23, 42).

The eastward routing hypothesis was challenged, however, by proxy salinity records (dynoflagellate cysts, $\delta^{18}O$) from the St. Lawrence estuary that indicated little increase in freshwater discharge during the Younger Dryas (43, 44), leading to other hypotheses including a short-lived (1-yr) flood from initial opening of the eastern Lake Agassiz outlet (45), LIS meltwater discharge and/or northward Lake Agassiz routing to the Arctic Ocean (46-48). Some have argued that potential eastward outlets were not deglaciated by the beginning of the YD (49), implying that Lake Agassiz did not drain during the Younger Dryas, but simple hydrological arguments demonstrate that the lake must have drained during the Younger Dryas (29).

A clear Younger Dryas salinity signal in the St. Lawrence estuary $\delta^{18}O$ record is identified when accounting for the effects of the local 5-10°C cooling and of ice volume (50).

Moreover, a reassessment finds that the dynoflagellate-cyst transfer function is not sensitive to salinity changes above a mean value of 12 practical salinity units (51), or at all (52). Additional runoff proxies provide further support for eastward routing to the St. Lawrence during the Younger Dryas (53) with a base-flow discharge increase of ~0.11 Sv (50) (Fig. 2I). With regard to the alternative hypotheses, we note that models indicate little or no ocean/climate response to the postulated Younger Dryas floods from Lake Agassiz (54, 55), and existing marine records do not indicate an increase in freshwater discharge to the Arctic at the start of the Younger Dryas (17, 56).

3. Data Analysis

We compiled 166 published proxy records of either temperature (sea surface or continental) or precipitation for the 20-11 ka interval (Table S1). Only records of moderate to high resolution (<500 yrs) and with at least several radiometric dates were included. The continental proxies record either temperature (n=50) or precipitation (n=29), and the marine proxies record either sea surface temperatures (SSTs) (n=74) or further information on temperature (n=3) or hydrological (n=10) variability from adjacent continents. SST records used here are based primarily on alkenones ($U^{K'}_{37}$) (n=34) and foraminiferal Mg/Ca (n=26), with the remainder from bioassemblages (n=6) and TEX_{86} (n=3), plus an additional 5 records that do not have calibrated temperatures (i.e., percent *N. pachyderma*). The records are from all ocean basins, although their distribution is skewed to the ocean margins. Below we evaluate potential bias in our results from this distribution.

Data density

We obtained the radiometric dates for 114 of the records used in our analysis (107 ^{14}C-based records, 7 ^{230}Th-based records). There are 640 dates from 20-11 ka and their distribution through time is shown in Figure S1. We used the published age models for the remaining 52 records: 16 are ice cores, 11 are based on tuning, 7 are regional composites based on multiple records, and we were unable to obtain the raw data for 18 records. Likewise, the density of proxy data points from all 166 records used in this study is plotted from 20-11 ka in Figure S1; there are >13,000 data points in total.

Age models

We recalibrated the age models for all radiocarbon-based records whose raw data were available or could be obtained from the original author (n=107). Radiocarbon ages were calibrated with the IntCal09 calibration (57) using the reservoir corrections suggested by the original authors. Age models were linearly interpolated between dates. Inverted dates within error of each other were averaged such that age models passed through the error bars of both dates. For non-radiocarbon-based records (e.g., ice cores, speleothems, tuned records) and records with unavailable raw data, the published age models were used.

Sea surface temperatures

We evaluated SST reconstructions from regional ocean basins, including the possibility of systematic biases between different proxies (Fig. S2). In any given basin, there is considerable variation among the specific proxy reconstructions as well as between the different proxies, particularly with regard to the structure and timing of SST changes. Differences between Mg/Ca and alkenone-based SST reconstructions, which account for most of the data, exist in some sites, but averaging of sites within regions suggest that the proxy differences are not systematic within analytical and calibration uncertainties (Fig. S2). One example of a clear proxy mismatch, however, comes from the North Atlantic basin, where the general agreement between alkenone and Mg/Ca SST reconstructions stands in marked contrast to those based on planktonic foraminifera (Fig. S2o-S2r).

4. Empirical Orthogonal Functions

We use empirical orthogonal functions (EOFs) to provide an objective characterization of deglacial climate variability. Because the records used here are based on various proxies and thus have widely ranging variances in their original units, we standardized each one to zero mean and unit variance prior to calculating EOFs. This standardization causes each record to provide equal 'weight' toward the EOFs. Note that for the SST EOF analysis, records were kept in degrees Celsius and thus their original variance was preserved. Records were interpolated to 100-yr resolution for all analyses.

Recalculating the PCs separately for Mg/Ca and alkenone records indicates general proxy agreement, although there are some systematic differences. In PC1, for example Mg/Ca-based SSTs show greater warming than alkenones between 18 and 16 ka and less warming between 12 and 10 ka (Fig. 3A). In PC2, although the overall pattern is similar for Mg/Ca and alkenone reconstructions (Fig 3B), the Mg/Ca reconstruction includes more short-term variations, with two cold anomalies at 16.6 ka and 14.6 ka, separated by warmth centered at 16.0 ka and terminated by abrupt warming at 14.4 ka, whereas the alkenones have a cool event that peaks at 16.9 ka, and abrupt warming at 14.7 ka. Finally, the PC2 for the Mg/Ca records suggest a much larger warming at the end of the Younger Dryas than seen in the PC2 for the alkenone records.

The leading EOF explains the vast majority of variance for most analyses, ranging from 44-97%, whereas EOF2 is relatively large in many analyses, ranging from 2-31%. Higher order modes usually account for <5% of the variance (Fig. S3) and have no systematic spatial patterns, suggesting that they most of them are likely insignificant. Accordingly, we show the two leading EOFs for all analyses in Figure 4, recognizing that in some cases the second EOF may be insignificant and that in other cases even higher order EOFs may be significant. We note, however, that these two leading EOFs account for at least two-thirds of the variance in all analyses (64-100%), and thus succinctly capture much or most of the variability in deglacial climate records.

5. Modeling records with principal components

We model the proxy records as the weighted sum of the first two principal components from each regional EOF analysis to show how well the leading modes for each region represent

the records (Figure S8). In other words, record x is modeled as PC1*EOF1$_x$ + PC2*EOF2$_x$, where EOF$_x$ is the loading for record x.

6. Principal components uncertainty estimates

We used a Monte Carlo procedure to derive error bars for the principal components shown in Figure 4 and 5, which reflect uncertainties in the proxy records. The principal components were calculated 1000 times after perturbing the records with chronological errors, and in the case of calibrated proxy temperature records (e.g., Mg/Ca, $U^{K'}_{37}$), with random temperature errors as well. The standard deviation of these 1000 realizations provides the 1σ error bars for the principal components.

We estimated chronological uncertainties for records based on radiometric dating (^{14}C and ^{230}Th; n=114) from errors on the dates as well as interpolation uncertainty between dates using a random walk model (58) with a jitter value of 188. We used published chronological uncertainties for the NGRIP, GRIP, EDML, and Dome C ice cores from(3) and(59). 1% chronological uncertainty (1σ) was assumed for other Greenland ice core records (n=3) and speleothem records whose raw data were unavailable (n=7). For the remaining 37 records, including other Antarctic ice cores, records based on tuning, and records without available raw data, we applied the average chronological uncertainty of the records with quantifiable uncertainties, which is ~2% (Figure S9). Proxy temperature records were perturbed with errors using quoted calibration uncertainties.

7. Robustness of SST PCs

The 69 calibrated high-resolution SST records used in this study are strongly biased toward ocean margins, owing to the relatively high sedimentation rates there. Furthermore, 43 records come from the Northern Hemisphere, whereas only 26 are from the Southern Hemisphere. We evaluate the question of how well the PCs derived from these records represent global ocean variability in four ways.

Jackknifing

We used a jackknifing approach in which 68% and 95% of the records were randomly excluded 1000 times and the PCs were recalculated. The standard deviation of the resulting 1000 PCs provides a measure of how sensitive the modes are to the number of input records. The results suggest that a leading mode dominated by a two-step warming pattern and a second mode characterized by the Oldest Dryas-Bølling/Allerød-Younger Dryas millennial oscillations are relatively robust and unlikely to change substantially with the inclusion of more records in the future (Figure S10).

Northern Hemisphere bias

To explore how significantly the Northern Hemisphere bias of the SST records may affect the extracted modes of variability we recalculated PCs after including the 26 Southern Hemisphere records twice (i.e., using the 43 Northern Hemisphere records, and the 26 Southern Hemisphere records twice, for a total of 95 time series). The PCs and the percentage of variance

they explain are nearly identical (Figure S11), suggesting the Northern Hemisphere bias of the records has little effect on the deglacial SST modes presented here.

Upwelling bias

The predominance of ocean margin records in our dataset may cause the modes of variability to be overprinted by local, upwelling signals rather than reflect global open-ocean SST variability. We calculated separate PCs for records from upwelling (n=19) and open-ocean (n=50) locations. Similar temporal modes of variability are obtained and the leading two modes explain ~80% of the variance in both cases (Figure S12). Interestingly, however, the relative order of the modes appears reversed, such that the two-step deglacial warming mode dominated at open-ocean sites whereas the millennial-scale oscillation mode was expressed more strongly at upwelling sites. Despite this difference, the similarity of these two leading PCs to each other, as well as to the two leading PCs obtained from the full SST database, suggests the SST modes identified here are not biased by local upwelling effects.

Instrumental data

The instrumental record of the past 140 years provides an opportunity to assess how well 69 locations are able to capture global SST variability. We calculated the leading two PCs for 69 random locations from the 1°x1° HadSST2 dataset (60) 1000 times. The standard deviations of the resulting 1000 PCs are much smaller than the variability of the PCs, suggesting 69 locations may be sufficient to approximate global variability. PCs derived from the specific locations of the 69 deglacial SST records are similar, though not identical, to the global PCs, suggesting the proxy site locations may capture a global signal reasonably well (Figure S13). It is important to emphasize, however, that 20th century and deglacial forcings were clearly different, and we thus acknowledge that the spatial relationships in the SST response may have been significantly different.

8. Deep Ocean

Records of the kinematic tracer $^{231}Pa/^{230}Th$ from deep North Atlantic sites show similar LGM values as in core-top sediments (Fig. 3E), suggesting a vigorous southward transport of NADW similar to present (31, 61). This apparent conflict may now be resolved, however, whereby the North Atlantic LGM $^{231}Pa/^{230}Th$ values reflect a southern source with low values that was transported to the north by expansion of AABW (62).

Table S1: Proxy records. The category used for the regional EOF analysis in Figure 6 is given on the left. EOF loadings from the global analysis including all records are given on the right; the absolute value of the loadings has been standardized to reflect the fraction of variance in each record explained by the EOF.

#	Region	Location	Core	Proxy	Reference	Lat	Lon	Elev/ Depth	Global EOF1	Global EOF2
1	Greenland T	NGRIP, Greenland	-	ice core $\delta^{18}O$	Rasmussen et al., 2006	75.1	-42.3	2917	0.43	0.10
2	Greenland P	NGRIP, Greenland	-	ice core accumulation rate	Lemieux-Dudon et al., 2010	75.1	-42.3	2917	0.51	0.21
3	Greenland T	GISP2, Greenland	-	ice core $\delta^{18}O$	Alley, 2000	72.6	-38.5	3207	0.18	0.19
4	Greenland P	GISP2, Greenland	-	ice core accumulation rate	Alley, 2000	72.6	-38.5	3207	0.47	0.08
5	Greenland T	GRIP, Greenland	-	ice core $\delta^{18}O$	Rasmussen et al., 2006	72.5	-37.6	3200	0.11	0.15
6	Greenland T	Renland, Greenland	-	ice core $\delta^{18}O$	Vinther et al., 2008	71.3	-26.7	2340	0.56	0.13
7	Europe T	Lyngen, Norway	-	pollen	Bakke et al., 2005	69.7	20.0	50	0.01	0.05
8	Beringia T	Hanging Lake, Alaska	-	pollen	Cwynar, 1982	68.4	-138.4	500	0.83	0.00
9	Beringia T	Burial Lake, Alaska	-	chironomids	Kurek et al., 2009	68.4	-159.2	460	0.88	0.00
10	Beringia T	Kaiyak Lake, Alaska	-	pollen	Anderson, 1985	68.2	-161.4	190	0.79	-0.14
11	Beringia T	Eastern Beringia (A)	-	pollen	Viau et al., 2008	67.5	-165.0	-	0.00	0.49
12	Beringia T	Eastern Beringia (B)	-	pollen	Viau et al., 2008	67.5	-137.5	-	0.59	0.00
13	Beringia T	Ranger Lake, Alaska	-	pollen	Brubaker et al., 1983	67.1	-153.7	820	0.60	-0.32
14	Beringia T	Joe Lake, Alaska	-	pollen	Anderson, 1988	66.8	-157.2	183	0.83	0.01
15	Beringia T	Eastern Beringia (D)	-	pollen	Viau et al., 2008	62.5	-137.5	-	0.00	0.22
16	Beringia T	Eastern Beringia (C)	-	pollen	Viau et al., 2008	62.5	-165.0	-	0.00	0.05
17	Beringia T	Zagoskin Lake, Alaska	-	chironomids	Kurek et al., 2009	60.5	162.1	7	0.65	-0.02
18	Beringia T	Arolik Lake, Alaska	-	BSi	Kaufman et al., 2003	59.5	161.1	145	0.61	0.06
19	N Atlantic T	North Atlantic	NA87-22	foram assemblages	Waelbroeck et al., 2001	55.5	-14.7	-2161	0.63	0.19
20	N Atlantic T	North Atlantic	VM23-81	N. pachy (s) %	Bond et al., 1999	54.3	-16.8	-2393	0.80	0.05
21	N Atlantic T	Northeast Atlantic	MD01-2461	foram Mg/Ca	Peck et al., 2008	51.8	-12.9	-1153	0.29	-0.30
22	Europe T	Feuenried, Germany	-	pollen	Rösch, 1997	47.8	8.9	395	0.48	0.33
23	Europe T	Rotsee, Switzerland	-	pollen	Ammann and Lotter, 1989	47.1	8.3	419	0.80	0.13
24	Europe T	Lobsigensee, Switzerland	-	pollen	Ammann, 1989	47.0	7.3	514	0.79	0.07

25	N America T	Davis Lake, Washington	-	pollen	Barnosky, 1981	46.6	-122.3	282	0.74	0.01
26	N America T	Battleground Lake, Washington	-	pollen	Whitlock, 1992	45.8	-122.5	155	0.59	0.00
27	Europe T	Avrig, Romania	-	pollen	Tantau et al., 2006	45.7	24.4	400	0.09	0.02
28	N America T	Little Lake, Oregon	-	pollen	Worona and Whitlock, 1995	44.2	-123.6	217	0.86	0.02
29	N America T	Hedrick Pond, Wyoming	-	pollen	Whitlock and Bartlein, 1993	43.8	-110.6	2073	0.71	0.00
30	N Pacific T	California margin	W8709A-8TC	$U^{K'}_{37}$	Prahl et al., 1995	42.5	-127.7	-3111	0.56	0.02
31	Europe T	Lake Banyoles, Spain	-	pollen	Pérez-Obiol and Julia, 1994	42.1	2.8	172	0.63	0.09
32	N America T	Bear Lake, Utah/Idaho		pollen	Jimenez-Moreno et al., 2007	42.0	-111.3	1805	0.71	0.16
33	N Atlantic T	North Atlantic	CH69-09	foram assemblages	Waelbroeck et al., 2001	41.8	-47.4	-4100	0.12	0.72
34	N Pacific T	Northeast Pacific	ODP 1019	N. pachy (s) %	Mix et al., 1999	41.7	-124.9	-980	0.60	0.05
35	-	Sofular Cave, Turkey	-	speleothem $\delta^{18}O$	Fleitmann et al., 2009	41.4	31.9	700	0.40	0.40
36	N America T	Tannersville Bog, Pennsylvania	-	pollen	Watts, 1979	41.0	-75.3	277	0.02	0.08
37	Europe T	Lago Grande di Monticchio, Italy	-	pollen	Allen et al., 1999	40.9	15.6	656	0.53	0.17
38	N America T	Chatsworth Bog, Illinois	-	pollen	Nelson et al., 2006	40.7	-88.3	220	0.10	-0.01
39	N Pacific T	Japan margin	PC-6	$U^{K'}_{37}$	Minoshima et al., 2007	40.4	143.5	-2215	-0.30	0.39
40	N Atlantic T	Western Mediterranean	M39-008	$U^{K'}_{37}$	Cacho et al., 2001	39.4	-7.1	-576	0.55	0.00
41	N Atlantic T	Western Mediterranean	BS79-38	$U^{K'}_{37}$	Cacho et al., 2001	38.4	13.6	-1489	0.53	-0.01
42	N America T	Browns Pond, Virginia	-	pollen	Kneller and Peteet, 1993	38.2	-79.6	620	-0.55	0.03
43	N Atlantic T	Iberian margin	SU81-18	foram assemblages	Waelbroeck et al., 2001	37.8	-10.2	-3135	0.13	0.56
44	N Atlantic T	Iberian margin	MD95-2042	$U^{K'}_{37}$	Bard et al., 2002	37.8	-10.7	-3140	0.48	0.03
45	N America T	Jackson Pond, Kentucky	-	pollen	Wilkins et al., 1991	37.5	-85.7	212	-0.04	0.19
46	N Atlantic T	North Atlantic	MD95-2037	$U^{K'}_{37}$	Calvo et al., 2001	37.1	-32.0	-2630	0.00	0.03
47	Asia P	Central China	-	loess grain size	Sun et al., 2010	36.3	104.6	?	0.88	0.05
48	N America T	Rockyhock Bay, North Carolina	-	pollen	Whitehead, 1981	36.2	-76.7	6	0.58	-0.11
49	N Atlantic T	Alboran Sea	MD95-2043	$U^{K'}_{37}$	Cacho et al., 1999	36.1	-2.6	-1841	0.65	0.14

50	Europe T	Iberian margin	MD95-2043	pollen	Fletcher et al., 2010	36.1	-2.6	-1841	0.81	0.05
51	N Pacific T	North Pacific	MD01-2421	$U^{K'}_{37}$	Isono et al., 2009	36.0	141.8	-2224	-0.03	0.28
52	N America T	Anderson Pond, Tennessee	-	pollen	Delcourt, 1979	36.0	-85.5	305	0.97	0.00
53	-	Chinese loess plateau	Section MS2008E	MBT/CBT	Peterse et al., 2011	34.9	113.3	200	0.92	-0.01
54	N Pacific T	Santa Barbara Basin, California	ODP 893A	foram $\delta^{18}O$	Hendy et al., 2002	34.3	-120.0	-576.5	0.85	0.00
55	Africa P	Eastern Mediterranean	ODP 967	IRM	Larrasoana et al., 2003	34.1	32.7	-2553	-0.43	-0.07
56	N America T	Clear Pond, South Carolina	-	pollen	Hussey, 1993	33.8	-79.0	10	0.64	0.03
57	N Atlantic T	Bermuda Rise	OCE326-GGC5	foram Mg/Ca	Carlson et al., 2008	33.7	-57.6	-4550	0.17	0.13
58	N America P	Fort Stanton Cave, New Mexico	-	speleothem $\delta^{18}O$	Asmerom et al., 2010	33.3	-105.3	?	-0.25	-0.11
59	N Atlantic T	Blake outer ridge	KNR140-51GGC	foram Mg/Ca	Carlson et al., 2008	32.6	-76.3	-1790	-0.20	-0.23
60	N Pacific T	Japan margin	KT92-17 St. 14	$U^{K'}_{37}$	Sawada and Handa, 1998	32.6	138.6	-3252	0.59	0.05
61	Asia P	Hulu Cave, China	-	speleothem $\delta^{18}O$	Wang et al., 2001	32.5	119.2	100	0.28	0.56
62	N America P	Cave of the Bells, Arizona	-	speleothem $\delta^{18}O$ (ice vol corrected)	Wagner et al., 2010	31.8	-110.8	?	-0.75	0.00
63	Indian T	Nile Delta	GeoB 7702-3	TEX_{86}	Castañeda et al., 2010	31.7	34.1	-562	0.48	0.14
64	Asia P	Sanbao Cave, China	-	speleothem $\delta^{18}O$	Wang et al., 2008	31.7	110.4	1900	0.01	0.55
65	N Pacific T	Japan margin	KY07-04-01	foram Mg/Ca	Kubota et al., 2010	31.6	128.9	-758	0.61	0.03
66	N Pacific T	East China Sea	MD98-2195	$U^{K'}_{37}$	Ijiri et al., 2005	31.6	129.0	-746	0.37	0.18
67	Asia P	Soreq Cave, Israel	-	speleothem $\delta^{18}O$	Bar-Matthews et al., 2003	31.5	35.0	400	0.53	-0.06
68	N America P	Camel Lake, Florida	-	pollen	Watts et al., 1992	30.3	-85.0	20	0.62	-0.01
69	N Atlantic T	Gulf of Mexico	MD02-2575	foram Mg/Ca	Ziegler et al., 2008	29.0	-87.1	-847	0.86	0.00
70	Indian T	Red Sea	GeoB 5844-2	$U^{K'}_{37}$	Arz et al., 2008	27.7	34.7	-963	0.34	0.51
71	N America P	Lake Tulane, Florida	-	pollen	Grimm et al., 1993	27.6	-81.5	34	0.12	0.18
72	N Atlantic T	Gulf of Mexico	EN32-PC6	foram Mg/Ca	Flower et al., 2004	27.0	-91.3	-2280	0.80	-0.03
73	Africa P	NW Sahara	-	lake levels	Hoelzmann et al., 1998	25.0	-4.0	-	0.69	0.08
74	Africa P	Central Sahara	-	lake levels	Hoelzmann et al., 1998	25.0	21.5	-	0.32	0.04

75	Africa P	NE Sahara	-	lake levels	Hoelzmann et al., 1998	25.0	47.0	-	0.74	-0.11
76	Asia P	Arabian Sea	MD-04 2876	$\delta^{15}N$	Pichevin et al., 2007	24.6	64.0	-828	0.03	0.45
77	Asia P	Arabian Sea	SO90-111 KL	TOC	Schulz et al., 1998	23.1	66.5	-775	-0.26	0.44
78	N Atlantic T	Northwest African margin	ODP 658C	foram assemblages	deMenocal et al., 2000	20.8	-18.6	-2263	0.78	-0.07
79	N Atlantic T	Northwest African margin	ODP 658C	$U^{K'}_{37}$	Zhao et al., 1995	20.8	-18.6	-2263	-0.05	0.01
80	WT Pacific	South China Sea	17940	$U^{K'}_{37}$	Pelejero et al., 1999	20.1	117.4	-1968	0.82	-0.01
81	Asia P	South China Sea	17940	grain size	Wang et al., 1999	20.1	117.4	-1727	0.79	-0.11
82	WT Pacific	South China Sea	ODP 1144	foram Mg/Ca	Wei et al, 2007	20.1	117.6	-2037	0.66	-0.05
83	Asia P	Arabian Sea	RC27-14	$\delta^{15}N$	Altabet et al., 2002	18.3	57.7	-596	0.55	0.24
84	Indian T	Arabian Sea	74KL	$U^{K'}_{37}$	Huguet et al., 2006	14.3	57.3	-3212	0.94	0.01
85	Indian T	Arabian Sea	74KL	TEX_{86}	Huguet et al., 2006	14.3	57.3	-3212	0.16	-0.67
86	Asia P	Socotra Island, Yemen	-	speleothem $\delta^{18}O$	Shakun et al., 2007	12.5	54.0	400	0.59	0.08
87	N Atlantic T	Western tropical North Atlantic	M35003-4	$U^{K'}_{37}$	Rühlemann et al., 1999	12.1	-61.3	-1299	0.66	-0.21
88	N Atlantic T	Western Caribbean Sea	VM28-122	foram Mg/Ca	Schmidt et al., 2004	11.6	-78.4	-3623	0.75	0.00
89	Indian T	Arabian Sea	NIOP-905	$U^{K'}_{37}$	Huguet et al., 2006	10.8	51.9	-1567	0.51	-0.30
90	Indian T	Arabian Sea	NIOP-905	TEX_{86}	Huguet et al., 2006	10.8	51.9	-1567	0.46	-0.37
91	N Atlantic T	Cariaco Basin, Venezuala	PL07-39PC	foram Mg/Ca	Lea et al., 2003	10.7	-65.0	-790	0.25	0.04
92	S America P	Cariaco Basin, Venezuela	ODP 1002C	550nm reflectance	Peterson et al., 2000	10.7	-65.2	-893	0.28	0.40
93	Asia P	Arabian Sea	NIOP-905	Al %	Ivanochko et al., 2005	10.5	51.6	-1586	0.35	0.04
94	WT Pacific	Sulu Sea	MD97-2141	foram Mg/Ca	Rosenthal et al., 2003	8.8	121.3	-3633	0.80	0.00
95	ET Pacific T	Eastern equatorial Pacific	MD02-2529	$U^{K'}_{37}$	Leduc et al., 2007	8.2	-84.1	-1619	0.76	-0.01
96	ET Pacific T	Eastern equatorial Pacific	ME0005A-43JC	foram Mg/Ca	Benway et al., 2006	7.9	-83.6	-1368	0.71	-0.12
97	WT Pacific	South China Sea	MD01-2390	$U^{K'}_{37}$	Steinke et al., 2008	6.6	113.4	-1545	0.64	0.19
98	WT Pacific	South China Sea	MD01-2390	foram Mg/Ca	Steinke et al., 2008	6.6	113.4	-1545	0.84	-0.06
99	WT Pacific	West Pacific warm pool	MD98-2181	foram Mg/Ca	Stott et al., 2007	6.3	125.8	-2114	0.91	0.00
100	ET Pacific T	Eastern equatorial Pacific	KNR176-JPC32	$U^{K'}_{37}$	Pahnke et al., 2007	4.7	-78.0	-2200	0.00	0.65

101	Asia P	Borneo	-	speleothem $\delta^{18}O$	Partin et al., 2007	4.0	114.8	150	0.43	0.23
102	N Atlantic T	Gulf of Guinea	MD03-2707	foram Mg/Ca	Weldeab et al., 2007	2.5	9.4	-1295	0.92	0.00
103	N Atlantic T	Eastern equatorial Atlantic	GeoB 4905	foram Mg/Ca	Weldeab et al,. 2005	2.5	9.4	-1328	0.62	-0.02
104	Africa P	Gulf of Guinea	MD03-2707	foram Ba/Ca	Weldeab et al., 2007	2.5	9.4	-1295	0.67	0.02
105	ET Pacific T	Eastern equatorial Pacific	TR163-22	foram Mg/Ca	Lea et al., 2006	0.5	-92.4	-2830	0.66	-0.12
106	ET Pacific T	Eastern equatorial Pacific	ME0005A-24JC	$U^{K'}_{37}$	Kienast et al., 2006	0.0	-86.5	-2941	0.01	0.56
107	Africa T	Sacred Lake, Mt Kenya	-	MBT/CBT	Russell et al, unpublished	-0.2	37.3	2400	0.71	-0.10
108	ET Pacific T	Eastern equatorial Pacific	V21-30	$U^{K'}_{37}$	Koutavas and Sachs, 2008	-1.2	-89.7	-617	0.43	0.04
109	ET Pacific T	Eastern equatorial Pacific	V21-30	foram Mg/Ca	Koutavas et al., 2002	-1.2	-89.7	-617	0.02	-0.24
110	ET Pacific T	Eastern equatorial Pacific	V19-28	$U^{K'}_{37}$	Koutavas and Sachs, 2008	-2.4	-84.7	-2720	0.47	0.00
111	ET Pacific T	Eastern equatorial Pacific	V19-30	$U^{K'}_{37}$	Koutavas and Sachs, 2008	-3.4	-83.5	-3091	0.56	0.18
112	Africa P	Burundi highlands	-	pollen-inferred precip	Bonnefille and Chalie, 2000	-3.5	29.5	~2000	0.03	0.07
113	S Atlantic T	Brazilian margin	GeoB 3910	$U^{K'}_{37}$	Jaeschke et al., 2007	-4.2	-36.3	-2362	0.85	0.00
114	S America P	northeast Brazil margin	GeoB3911-3	Fe/Ca	Arz et al., 1998	-4.6	-36.6	-828	-0.06	-0.02
115	S Atlantic T	Western tropical Atlantic	GeoB 3129	foram Mg/Ca	Weldeab et al, 2006	-4.6	-36.6	-830	0.72	-0.14
116	WT Pacific	West Pacific warm pool	MD9821-62	foram Mg/Ca	Visser et al., 2003	-4.7	117.9	-1855	0.88	0.00
117	WT Pacific	West Pacific warm pool	MD98-2176	foram Mg/Ca	Stott et al., 2007	-5.0	133.4	-2382	0.90	0.01
118	S Atlantic T	Gulf of Guinea	GeoB 6518-1	$U^{K'}_{37}$	Schefuß et al., 2005	-5.6	11.2	-962	0.16	-0.03
119	Africa T	Gulf of Guinea	GeoB 6518-1	MBT/CBT	Weijers et al., 2007	-5.6	11.2	-962	0.78	0.11
120	Africa P	Gulf of Guinea	GeoB 6518-1	leaf wax δD	Schefuß et al., 2005	-5.6	11.2	-962	0.56	0.00
121	S America P	Rainha Cave, Brazil	-	speleothem $\delta^{18}O$	Cruz et al., 2009	-5.6	-37.7	100	0.36	-0.38
122	S America P	El Condor Cave, Peru	-	speleothem $\delta^{18}O$	Cheng et al., in prep.	-5.9	-77.3	860	-0.47	-0.18
123	Africa T	Lake Tanganyika	NP04-KH3	TEX_{86}	Tierney et al., 2008	-6.7	29.6	773	0.51	-0.01
124	Africa P	Lake Tanganyika	NP04-KH3	leaf wax δD	Tierney et al., 2008	-6.7	29.6	773	0.82	0.02
125	WT Pacific	West Pacific warm	MD98-2165	foram Mg/Ca	Levi et al., 2007	-9.7	118.4	-2100	0.77	-0.11

		pool								
126	Africa P	Lake Malawi	M98-2P	biogenic silica	Johnson et al., 2002	-10.0	34.2	500	-0.04	-0.48
127	Africa P	Lake Malawi	M98-1 and 2P	leaf wax d13C	Castañeda et al., 2007	-10.0	34.2	500	0.23	-0.09
128	WT Pacific	West Pacific warm pool	MD98-2170	foram Mg/Ca	Stott et al., 2007	-10.6	125.4	-832	0.91	-0.01
129	Africa T	Lake Malawi	MD98-1P, MD98-2P	TEX_{86}	Powers et al., 2005	-11.0	34.2	500	0.82	-0.02
130	WT Pacific	Timor Sea, Indian Ocean	MD01-2378	foram Mg/Ca	Xu et al., 2008	-13.1	121.8	-1783	0.88	-0.03
131	S America P	Lake Titicaca	NE-98-PC1	freshwater diatom %	Baker et al., 2001	-16.1	-69.1	3810	-0.03	-0.36
132	S Atlantic T	Southeast Atlantic	GeoB 1023-5	$U^{K'}_{37}$	Kim et al., 2002	-17.2	11.0	-1978	0.53	-0.35
133	Africa T	Southeast Atlantic	GeoB 1023	% Fynbos pollen	Ning Shi et al., 1998	-17.2	11.0	-1978	0.65	-0.23
134	Africa T	Lake Tritrivakely, Madagascar	-	% non-alpine pollen	Gasse and Van Campo, 1998	-19.8	46.9	1778	0.85	-0.01
135	Africa P	Lake Tritrivakely, Madagascar	-	% arboreal pollen	Gasse and Van Campo, 1998	-19.8	46.9	1778	0.39	-0.35
136	S America P	Salar de Uyuni, Bolivia	-	gamma radiation	Baker et al., 2001	-20.2	-67.5	3653	-0.67	-0.16
137	Indian T	Indian Ocean	MD79257	$U^{K'}_{37}$	Bard et al., 1997	-20.4	36.3	-1260	0.80	0.03
138	S Atlantic T	South Atlantic	GeoB 1711	N. pachy (s) %	Little et al., 1997	-23.6	12.4	-1967	0.69	-0.27
139	Africa P	Lake Tswaing, South Africa	-	Cl counts	Kristen et al., 2007	-25.4	28.1	1045	0.67	-0.01
140	S Atlantic T	Subtropical southeast Atlantic	ODP 1084B	foram Mg/Ca	Farmer et al., 2005	-25.5	13.0	-1992	0.19	-0.14
141	S America P	Caverna Botuvera	-	speleothem $\delta^{18}O$	Wang et al., 2007	-27.2	-49.2	250	-0.62	-0.32
142	S America P	Caverna Botuvera	-	speleothem $\delta^{18}O$	Cruz et al., 2005	-27.2	-49.2	230	-0.08	-0.23
143	S Atlantic T	Brazilian margin	KNR159-5-36GGC	foram Mg/Ca	Carlson et al., 2008	-27.5	-46.5	-1268	0.18	0.15
144	S Pacific T	Chilean margin	GeoB 7139-2	$U^{K'}_{37}$	Kaiser et al., 2008	-30.2	-72.0	-3270	0.94	0.01
145	S Pacific T	South Australia	MD03-2611	$U^{K'}_{37}$	Calvo et al., 2007	-36.7	136.7	-2420	0.77	-0.17
146	S Pacific T	New Zealand	MD97-2121	$U^{K'}_{37}$	Pahnke and Sachs, 2006	-40.4	178.0	-3014	0.90	0.00
147	S Atlantic T	Southeast Atlantic	ODP 1089	radiolaria assemblages	Cortese et al., 2002	-40.9	9.9	-4575	0.68	-0.04
148	S Pacific T	Chilean margin	ODP 1233	$U^{K'}_{37}$	Lamy et al., 2007	-41.0	-74.5	-838	0.81	-0.12
149	S Pacific T	New Zealand	-	speleothem $\delta^{18}O$ (ice vol corrected)	Williams et al., 2010	-41.0	172.0	170	0.38	-0.02

150	S Atlantic T	Southeast Atlantic	TN057-21-PC2	$U^{K'}_{37}$	Sachs et al., 2001	-41.1	7.5	-4981	0.95	-0.01
151	S Atlantic T	Southeast Atlantic	TN057-21	foram Mg/Ca	Barker et al., 2009	-41.1	7.8	-4981	0.24	-0.40
152	S Pacific T	New Zealand	-	speleothem $\delta^{18}O$	Hellstrom et al., 1998	-41.2	172.7	590	0.74	-0.01
153	S Atlantic T	South Atlantic	RC11-83	foram $\delta^{18}O$	Charles et al., 1996	-41.6	9.8	-4718	0.84	-0.12
154	S Pacific T	New Zealand	SO136-GC11	$U^{K'}_{37}$	Barrows et al., 2007	-43.5	167.9	-1556	0.69	-0.17
155	S Pacific T	New Zealand	MD97-2120	$U^{K'}_{37}$	Pahnke and Sachs, 2006	-45.5	174.9	-1210	0.87	0.02
156	Indian T	Southern Ocean	MD88-770	foram assemblages	Labeyrie et al., 1996	-46.0	96.5	-3290	0.37	-0.23
157	Antarctica T	Law Dome, Antarctica	-	ice core $\delta^{18}O$	Morgan et al., 2002	-67.0	113.0	1390	0.88	-0.03
158	Antarctica T	Talos Dome, Antarctica	-	ice core $\delta^{18}O$	Stenni et al., 2011	-72.8	159.2	2315	0.81	-0.10
159	Antarctica T	EDML, Antarctica	-	ice core $\delta^{18}O$	Stenni et al., 2010	-75.0	0.0	2892	0.88	-0.06
160	Antarctica P	EDML, Antarctica	-	ice core accumulation rate	Lemieux-Dudon et al., 2010	-75.0	0.0	2892	0.74	-0.13
161	Antarctica T	Dome C, Antarctica	-	ice core $\delta^{18}O$	Stenni et al., 2010	-75.1	123.4	3240	0.93	-0.02
162	Antarctica P	Dome C, Antarctica	-	ice core accumulation rate	Lemieux-Dudon et al., 2010	-75.1	123.4	3240	0.87	0.00
163	Antarctica T	Dome Fuji, Antarctica	-	ice core $\delta^{18}O$	Kawamura et al., 2007	-77.3	39.7	3810	0.92	-0.06
164	Antarctica T	Vostok, Antarctica	-	ice core δD	Petit et al., 1999	-78.5	108.0	3500	0.95	0.00
165	Antarctica T	Byrd, Antarctica	-	ice core $\delta^{18}O$	Blunier and Brook, 2001	-79.9	-119.4	1530	0.85	-0.04
166	Antarctica T	Siple Dome, Antarctica	-	ice core $\delta^{18}O$	Brook et al., 2005	-81.6	-148.8	621	0.91	0.00

Table S2: Rate of change of area of the Scandinavian Ice Sheet. Data provided by Richard Gyllencreutz and Jan Mangerud.

Age (ka)	Rate of area change (10^5 km^2 kyr^{-1})
9	2.51
10	5.36
11	8.42
12	1.62
13	6.35
14	8.80
15	5.66
16	4.04
17	6.11
18	4.14
19	-0.80
20	-0.21
21	-0.98
22	-4.74
23	-7.23
24	-2.78

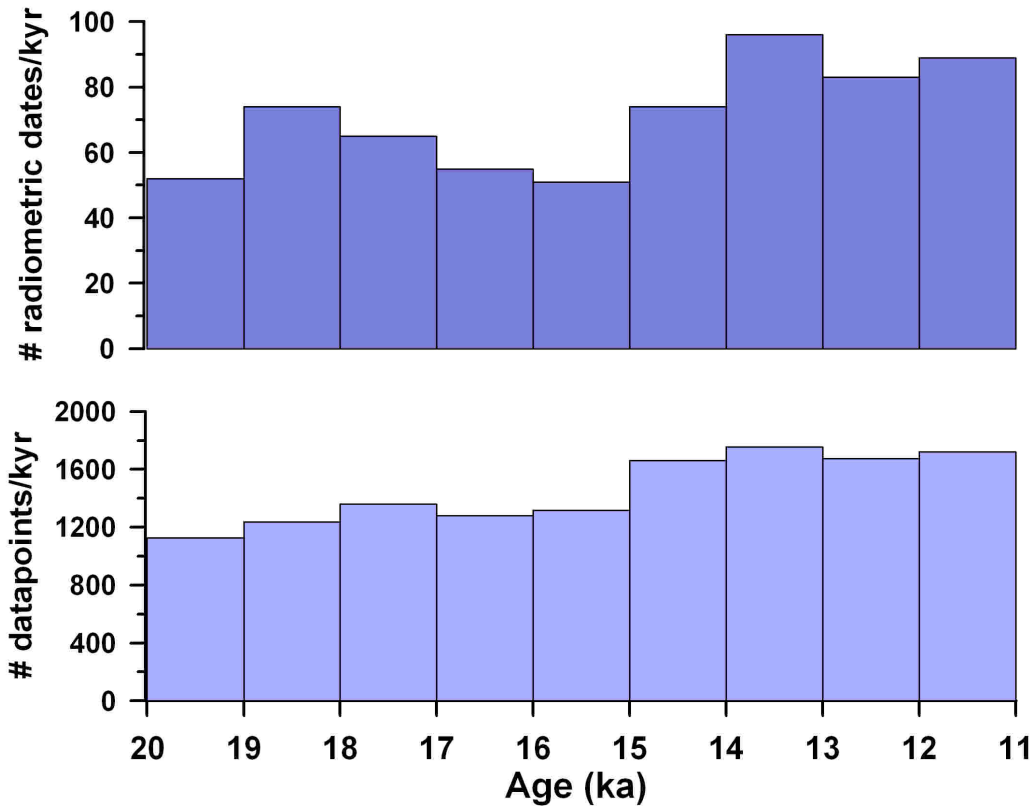

Figure S1: Histograms showing the number of radiometric dates and proxy data points in the data base binned in 1-kyr intervals.

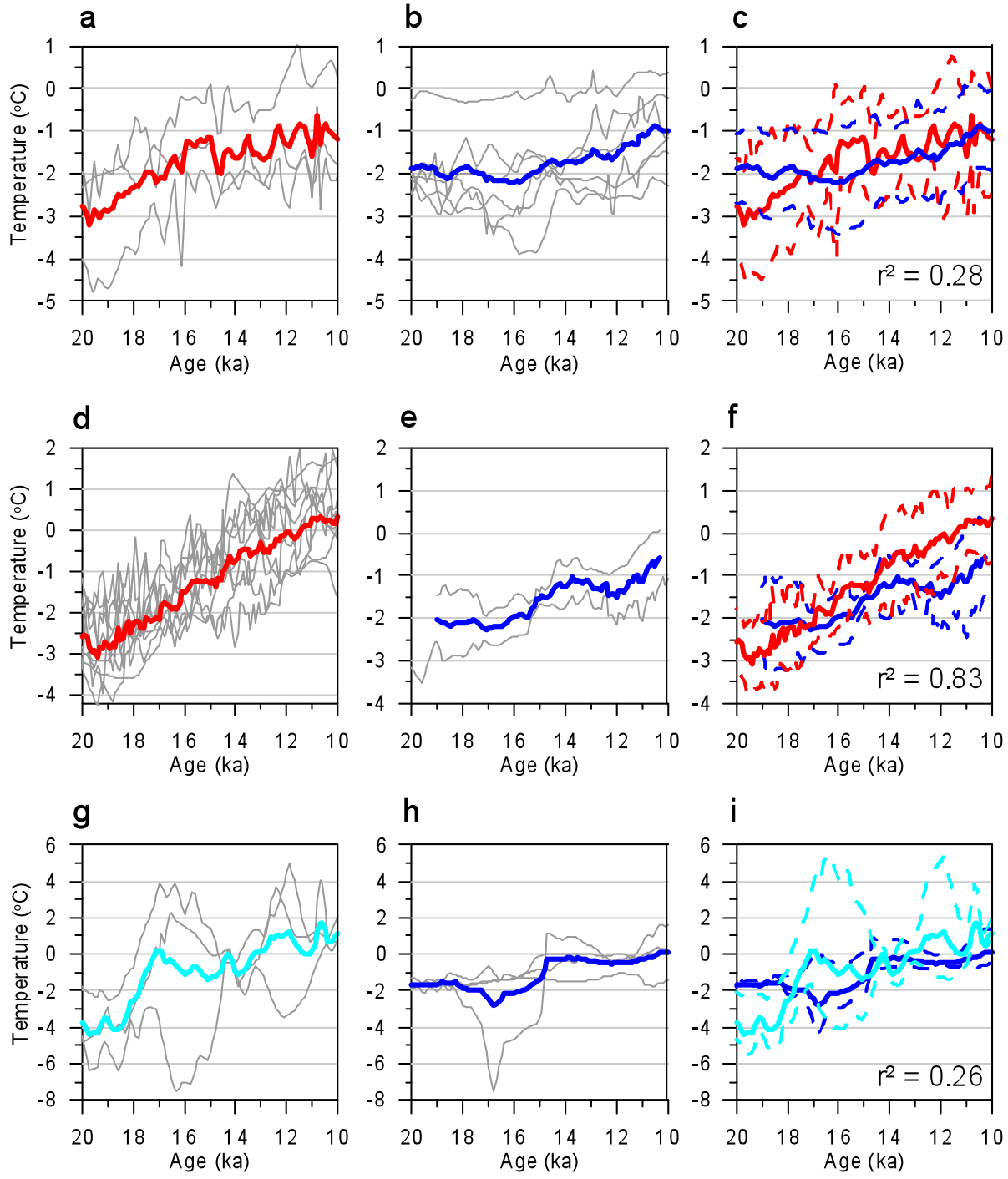

Figure S2.

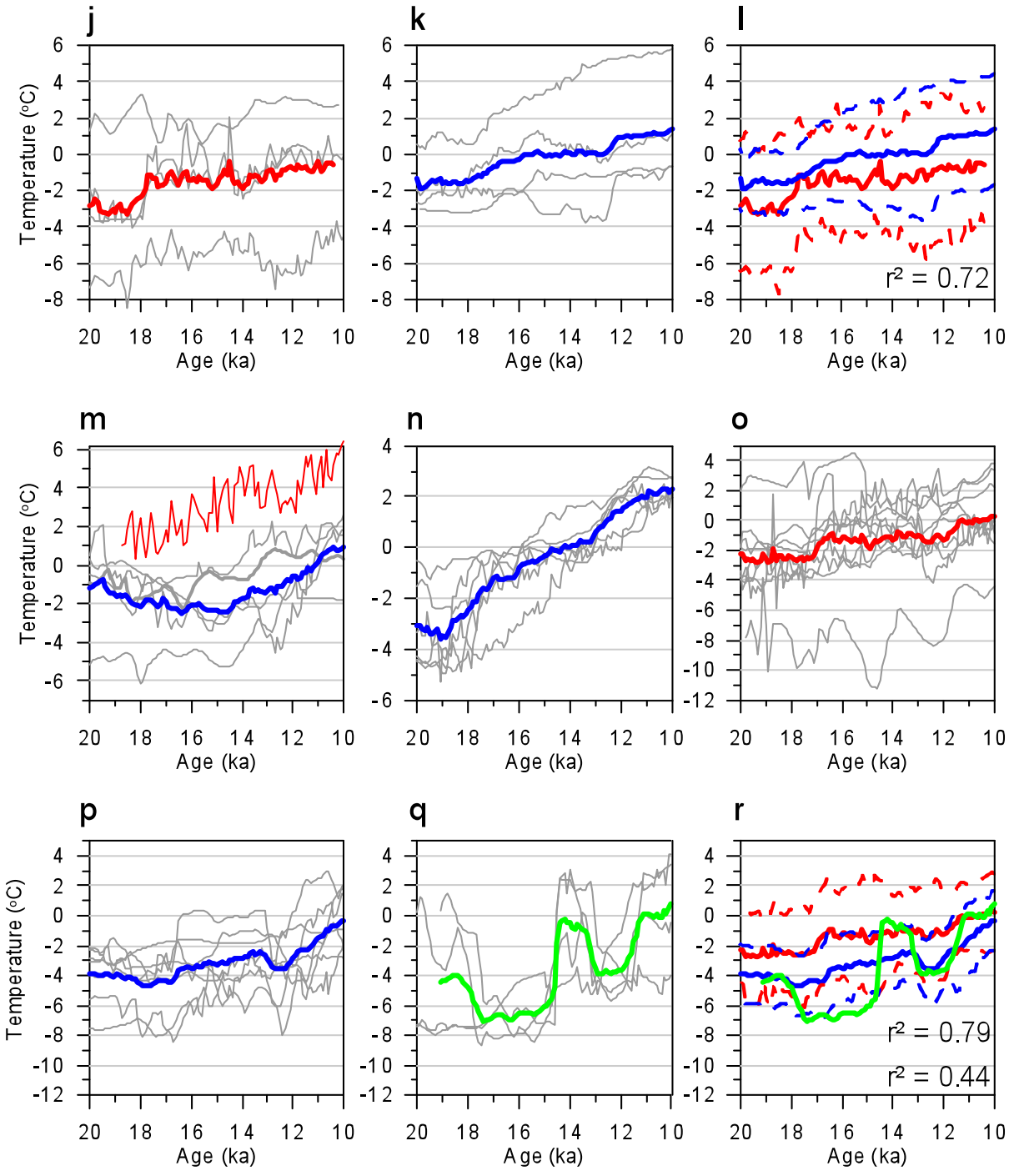

Figure S2 (continued).

Figure S2. Sea surface temperature data recalculated as anomalies from modern mean annual temp at each site (based on 1961-1990 AD climatology from 1x1 degree HadISST1 dataset (Rayner et al., 2006)). (**a**) Mg/Ca reconstructions from the eastern equatorial Pacific Ocean (gray lines) and their average (red line). (**b**) Alkenone ($U^{K'}_{37}$) reconstructions from the eastern equatorial Pacific Ocean (gray lines) and their average (blue line). (**c**) Comparison of Mg/Ca reconstruction (red line with 1 σ shown by dashed red lines) and alkenone ($U^{K'}_{37}$) reconstruction (blue line with 1 σ shown by dashed blue lines) from the eastern equatorial Pacific Ocean. Correlation (fraction of shared variance, r^2) between two averages is shown. (**d**) Mg/Ca reconstructions from the western equatorial Pacific Ocean (gray lines) and their average (red line). (**e**) Alkenone ($U^{K'}_{37}$) reconstructions from the western equatorial Pacific Ocean (gray lines) and their average (blue line). (**f**) Comparison of Mg/Ca reconstruction (red line with 1 σ shown by dashed red lines) and alkenone ($U^{K'}_{37}$) reconstruction (blue line with 1 σ shown by dashed blue lines) from the western equatorial Pacific Ocean. Correlation (r^2) between two averages is shown. (**g**) TEX_{86} reconstructions from the Indian Ocean (gray lines) and their average (light blue line). (**h**) Alkenone ($U^{K'}_{37}$) reconstructions from the Indian Ocean (gray lines) and their average (blue line). (**i**) Comparison of TEX_{86} reconstruction (light blue line with 1 σ shown by dashed light blue lines) and alkenone ($U^{K'}_{37}$) reconstruction (blue line with 1 σ shown by dashed blue lines) from Indian Ocean. Correlation (r^2) between two averages is shown. (**j**) Mg/Ca reconstructions from the South Atlantic Ocean (gray lines) and their average (red line). (**k**) Alkenone ($U^{K'}_{37}$) reconstructions from the South Atlantic Ocean (gray lines) and their average (blue line). (**l**) Comparison of Mg/Ca reconstruction (red line with 1 σ shown by dashed red lines) and alkenone ($U^{K'}_{37}$) reconstruction (blue line with 1 σ shown by dashed blue lines) from South Atlantic Ocean. Correlation (r^2) between two averages is shown. (**m**) Alkenone ($U^{K'}_{37}$) reconstructions from the North Pacific Ocean (gray lines) and their average (blue line) compared to one Mg/Ca record (red line). (**n**) Alkenone ($U^{K'}_{37}$) reconstructions from the South Pacific Ocean (gray lines) and their average (blue line). (**o**) Mg/Ca reconstructions from the North Atlantic Ocean (gray lines) and their average (red line). (**p**) Alkenone ($U^{K'}_{37}$) reconstructions from the North Atlantic Ocean (gray lines) and their average (blue line). (**q**) Foraminiferal reconstructions from the North Atlantic Ocean (gray lines) and their average (green line). (**r**) Comparison of Mg/Ca reconstruction (red line with 1 σ shown by dashed red lines), alkenone ($U^{K'}_{37}$) reconstruction (blue line with 1 σ shown by dashed blue lines), and foraminiferal reconstruction (green line) from North Atlantic Ocean. Correlation (r^2) between two averages is shown: $r^2 = 0.79$ is between Mg/Ca and alkenone reconstructions, $r^2 = 0.44$ is between Mg/Ca and foraminiferal reconstructions.

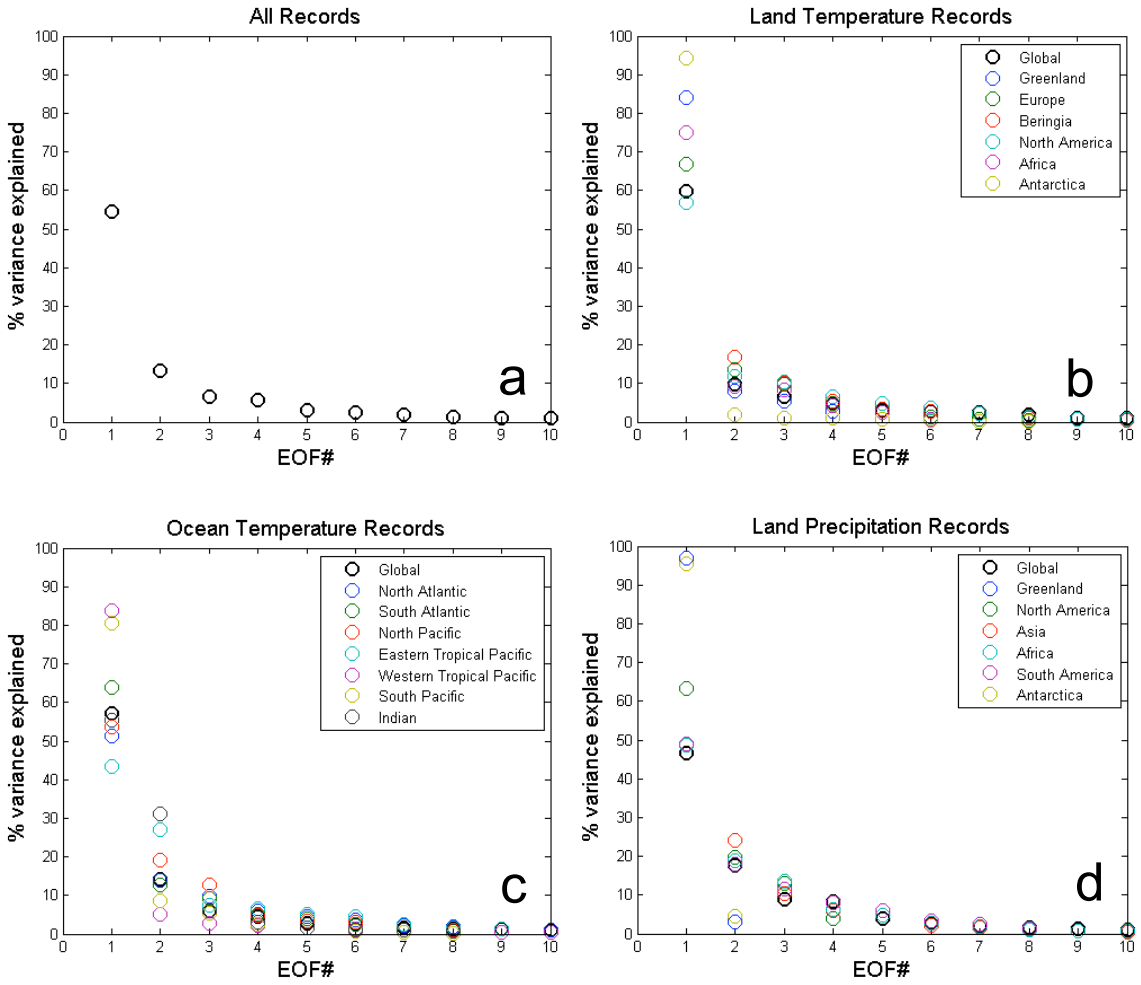

Figure S3: The percentage of variance explained by the first 10 EOFs for each regional (color circles) and global (bold black circles) analysis shown in Figure 4 in the main text. (**a**) All records, (**b**) land temperature records, (**c**) ocean temperature records, (**d**) land precipitation records.

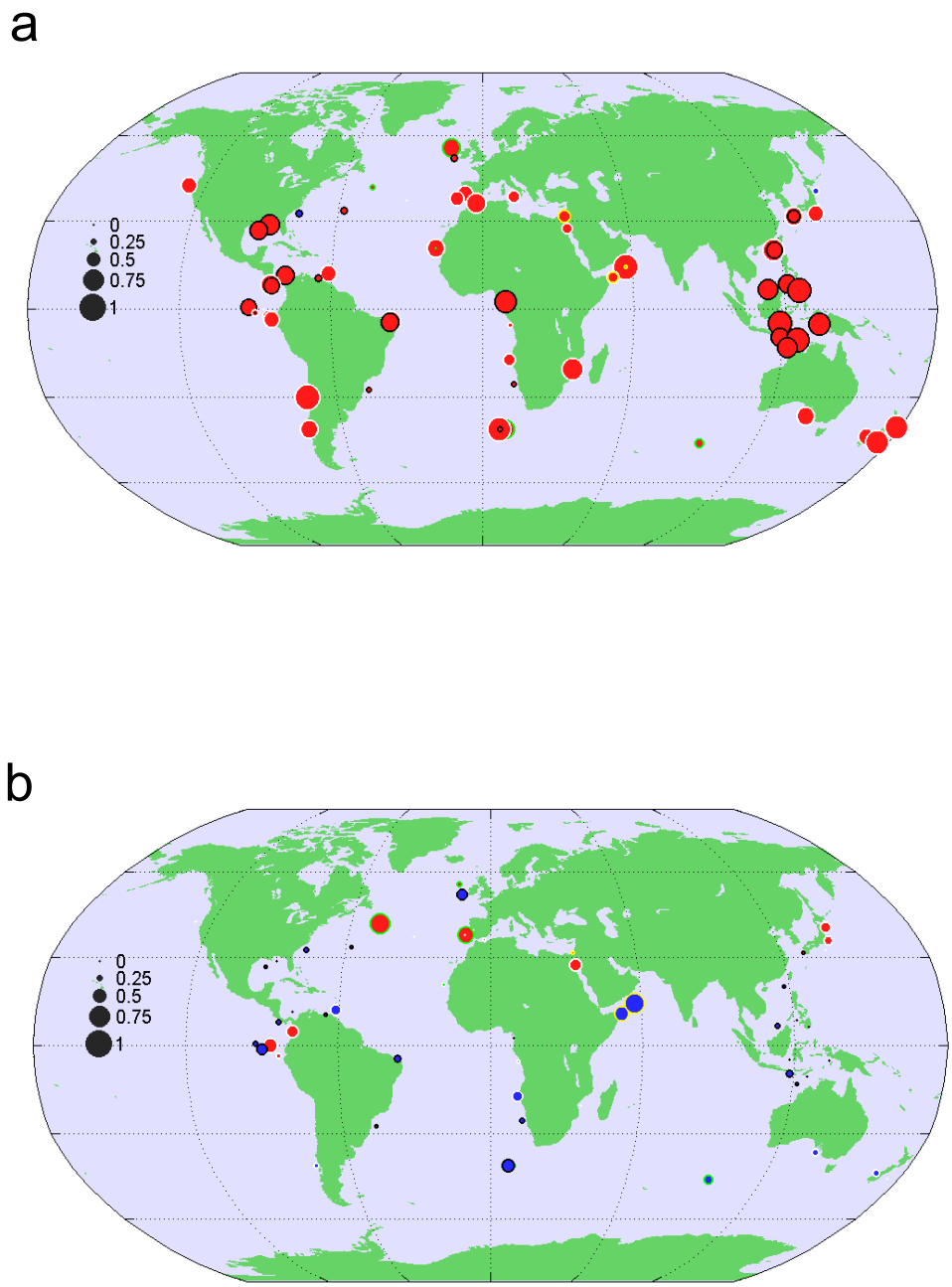

Figure S4: Factor loadings for the fraction of variance in each record explained by the leading mode of deglacial SST variability. (**a**) EOF1 and (**b**) EOF2. Positive EOF loadings are shown in red and negative loadings are blue, and the EOF loadings have been scaled to reflect the fraction of variance explained by the PC. Loading outline color symbolizes proxy type: Mg/Ca = black; $U^{K'}_{37}$ = white; TEX_{86} = yellow; bioassemblage = green. Some sites include more than one record, as indicated by smaller circles inset in larger circles.

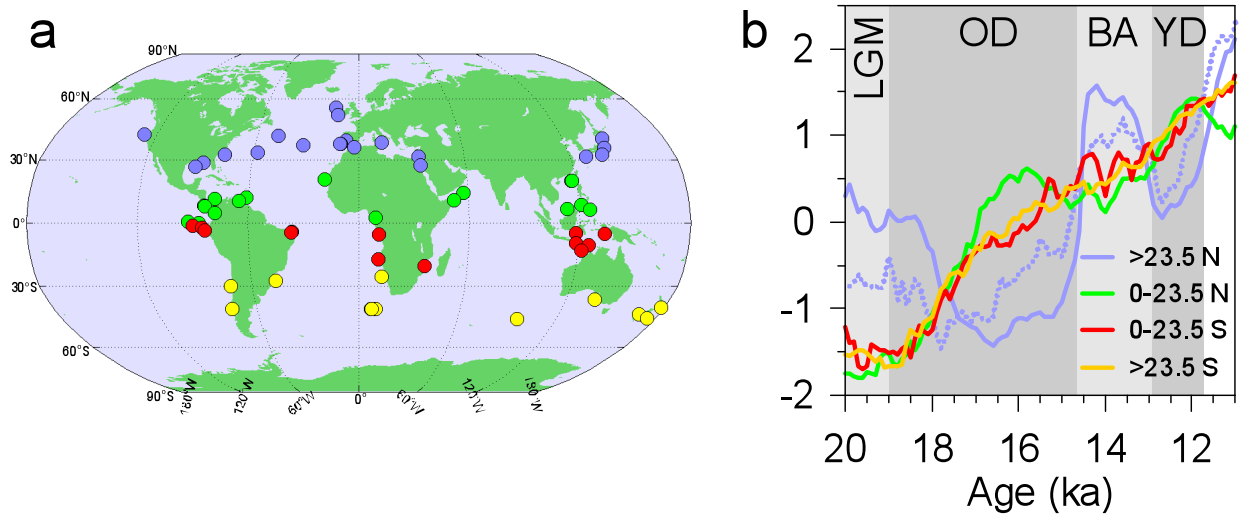

Figure S5: (**a**) Map showing sites used for PCs shown in (**b**), color coded the same way. (**b**) The leading PCs for the tropics and extratropics of each hemisphere. >23.5°N = light blue line, 0-23.5°N = green line, 0-23.5°S = red line, >23.5°S = orange line. Percentage of variance explained by each PC is 56% for >23.5°N, 68% for 0-23.5°N, 79% for 0-23.5°S, and 79% for >23.5°S. PCs have been standardized to unit variance to facilitate comparison.

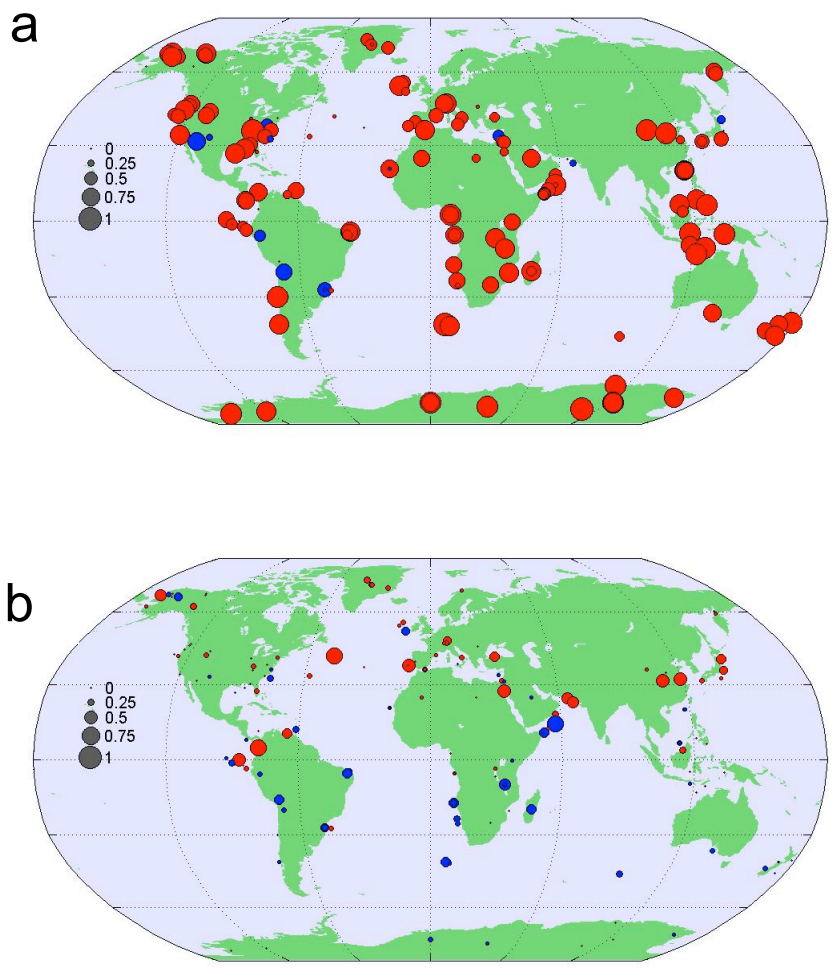

Figure S6: (**a**) EOF1 and (**b**) EOF2 from the global EOF analysis. Positive EOF loadings are shown in red and negative loadings are blue, and their magnitude is represented by symbol size. EOF loadings have been scaled to reflect the fraction of variance explained by the PC.

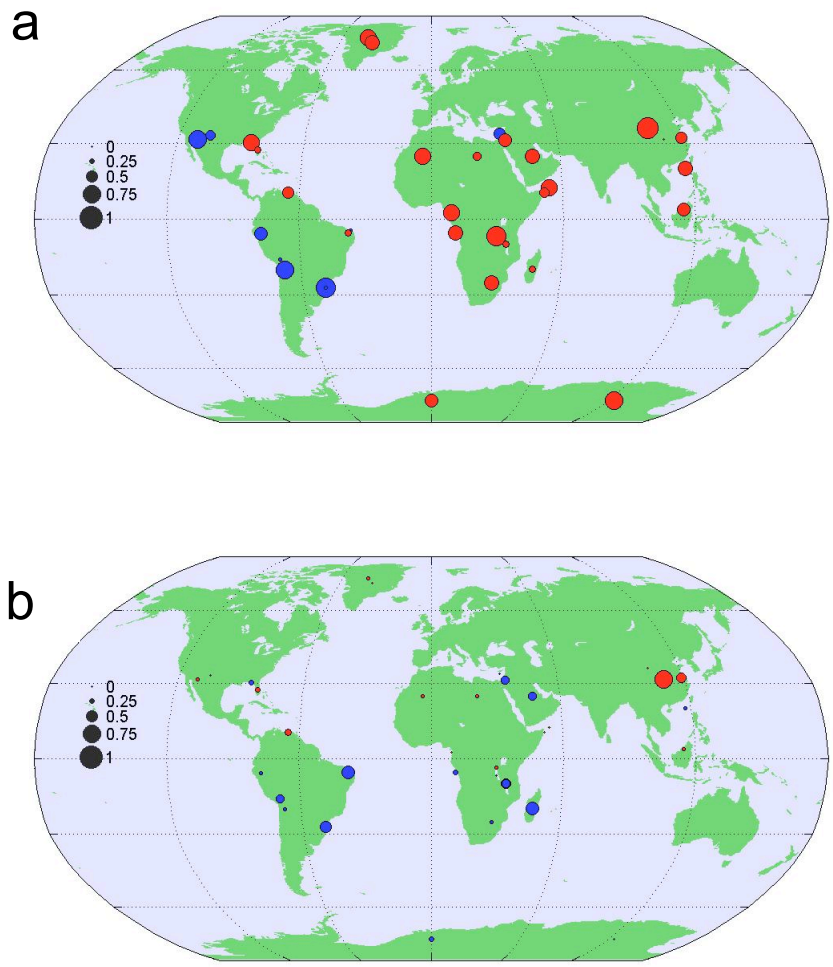

Figure S7: (**a**) EOF1 and (**b**) EOF2 from the land-precipitation EOF analysis. Positive EOF loadings are shown in red and negative loadings are blue, and their magnitude is represented by symbol size. EOF loadings have been scaled to reflect the fraction of variance explained by the PC.

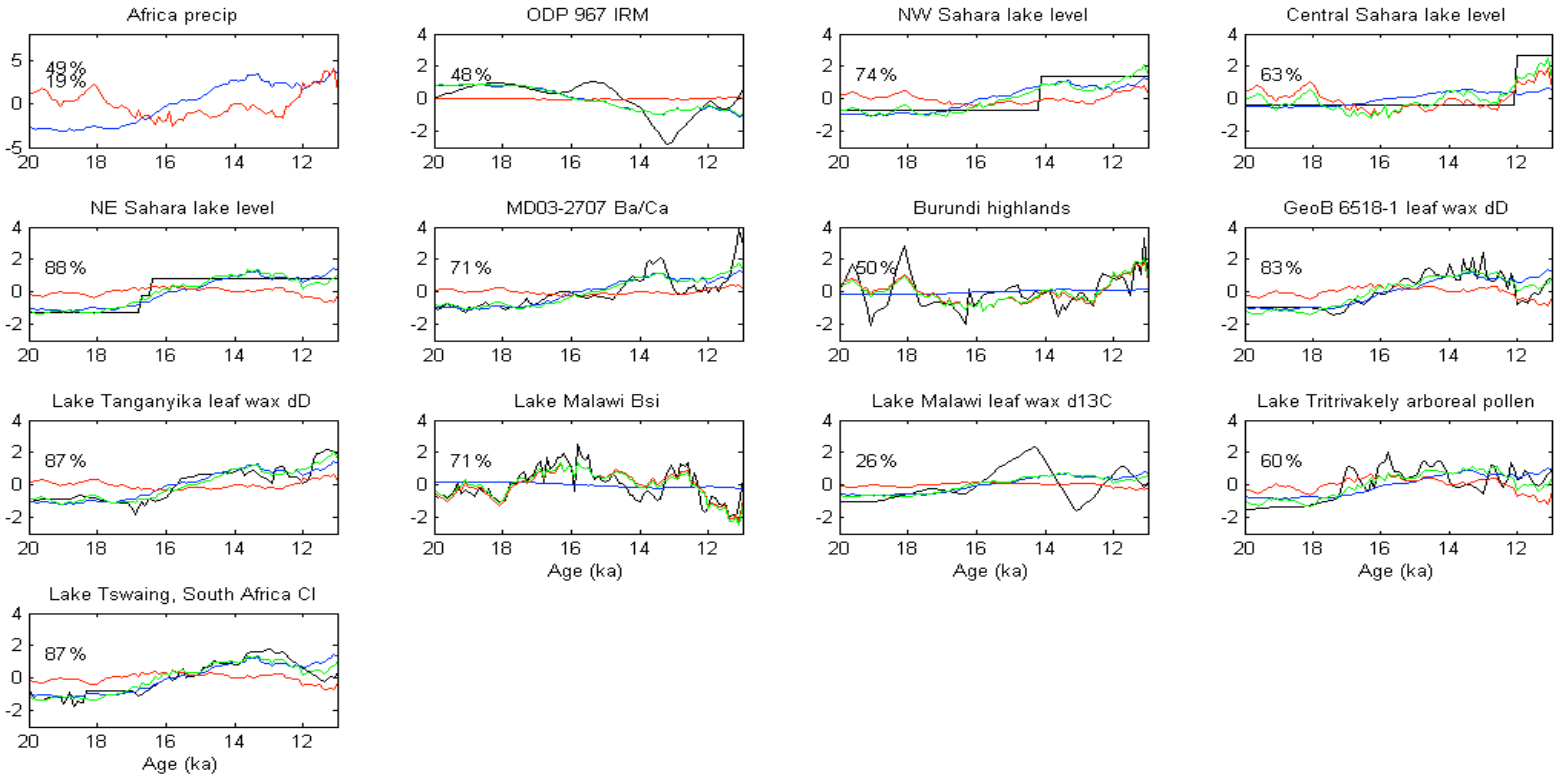

Figure S8. Records modeled as the weighted sum of the first two principal components for each region. Each panel corresponds to a different regional analysis. For each panel, PC1 (blue) and PC2 (red) for the region and the percentage of variance they explain are shown in the upper left plot. The other plots in each panel show the original proxy records (black), PC1 (blue) and PC2 (red) weighted by the records' EOF loadings, and the sum of these weighted PCs (green). The percentage of variance of each record explained by the first two EOFs is given in the upper left corner of each plot. Note that all records have been standardized to mean zero, unit variance.

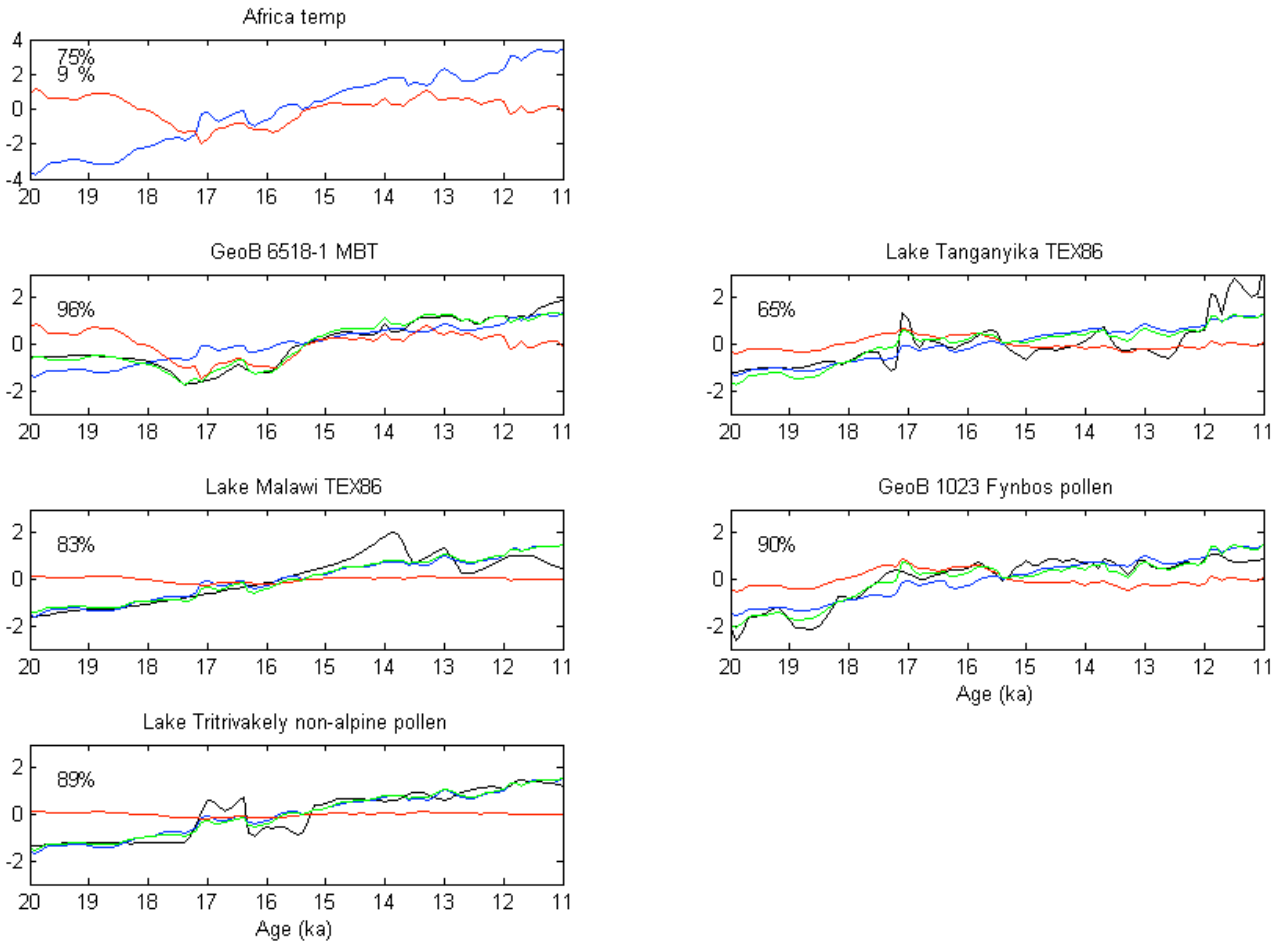

Figure S8 (continued).

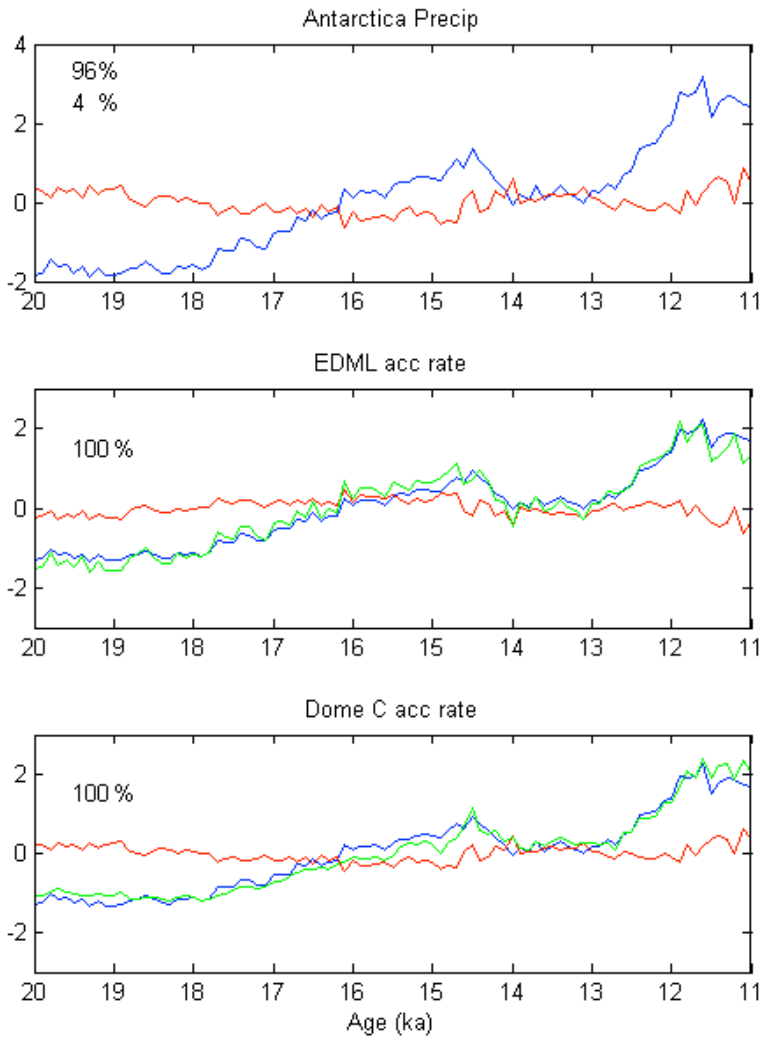

Figure S8 (continued).

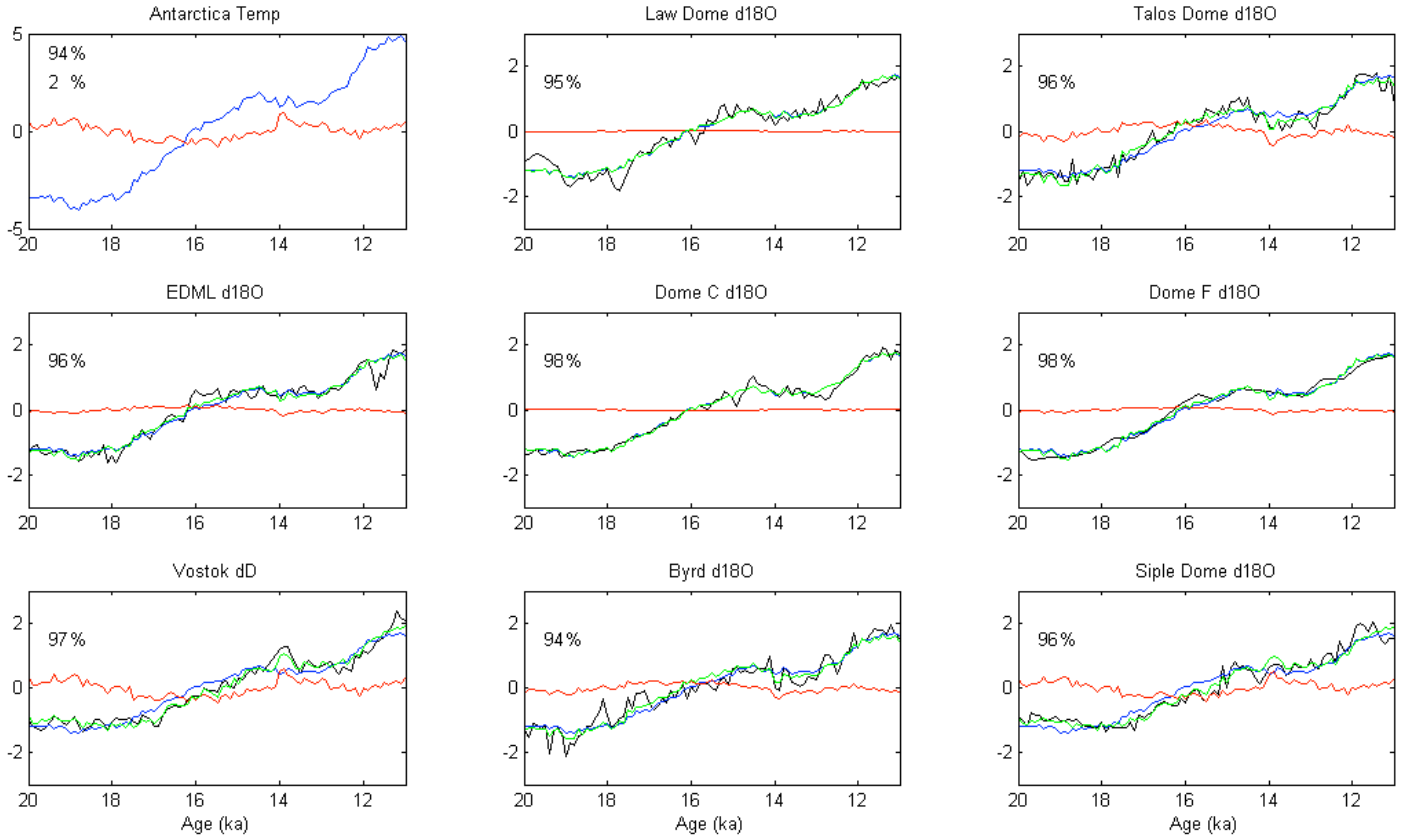

Figure S8 (continued).

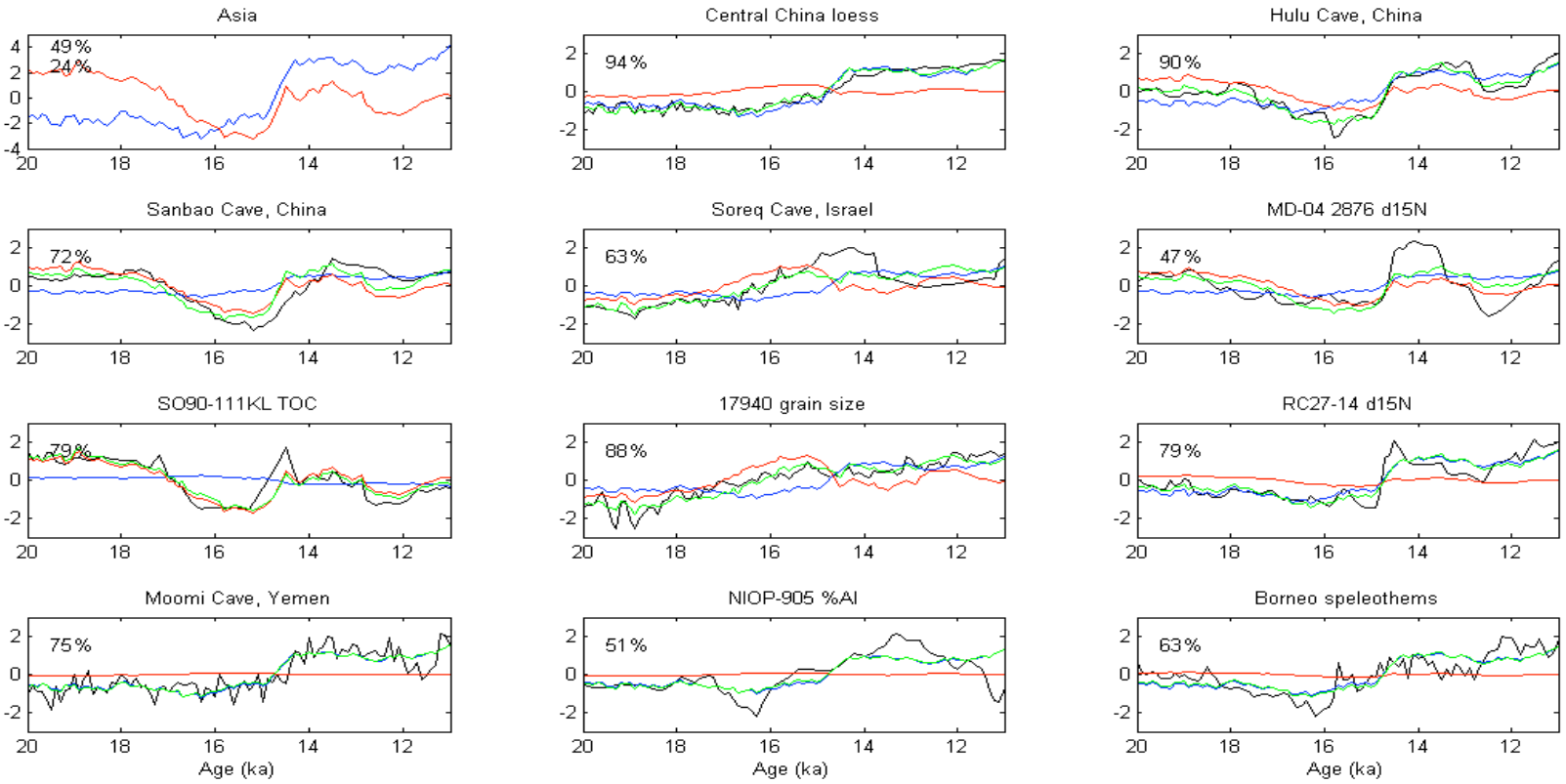

Figure S8 (continued).

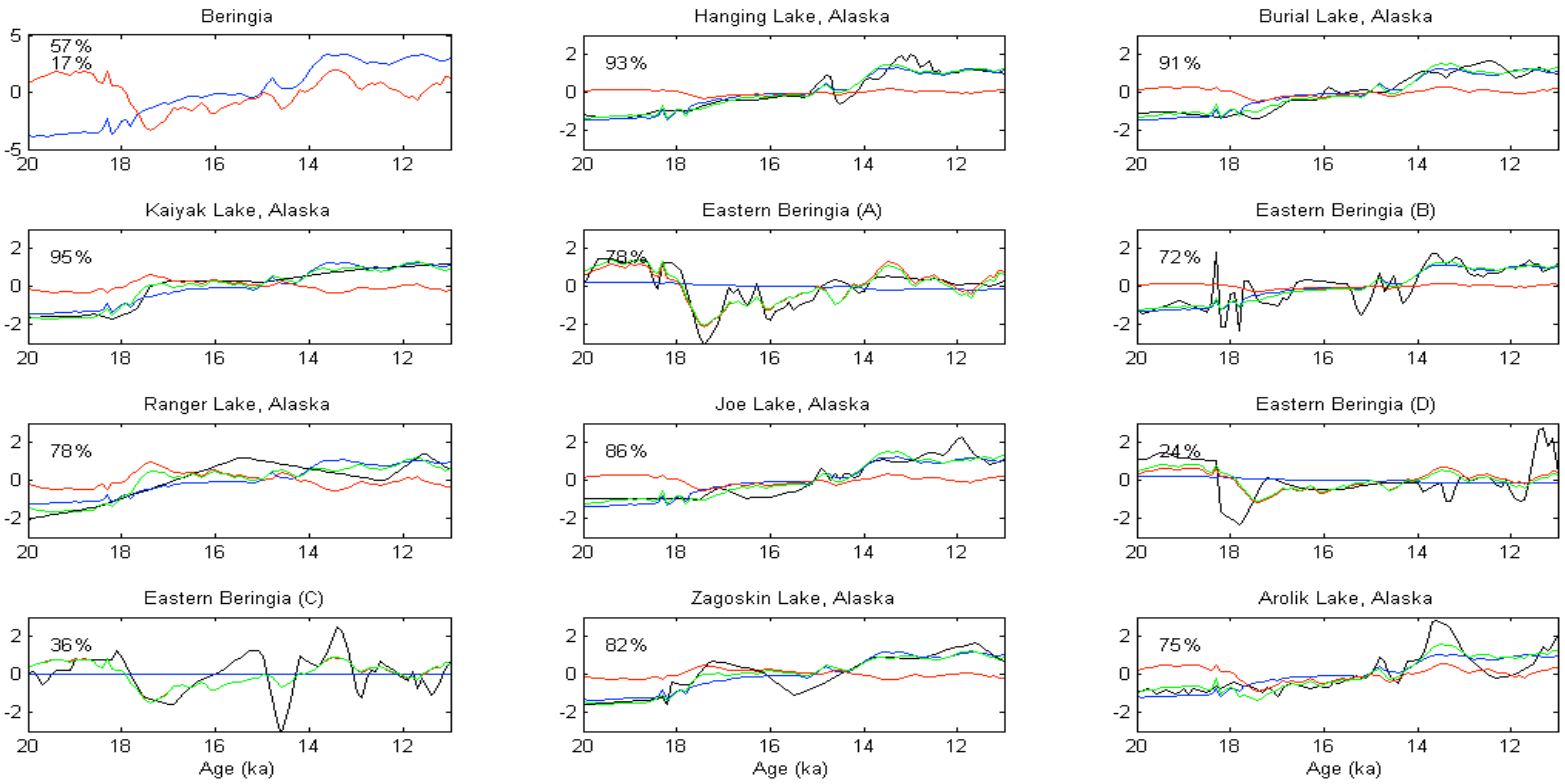

Figure S8 (continued).

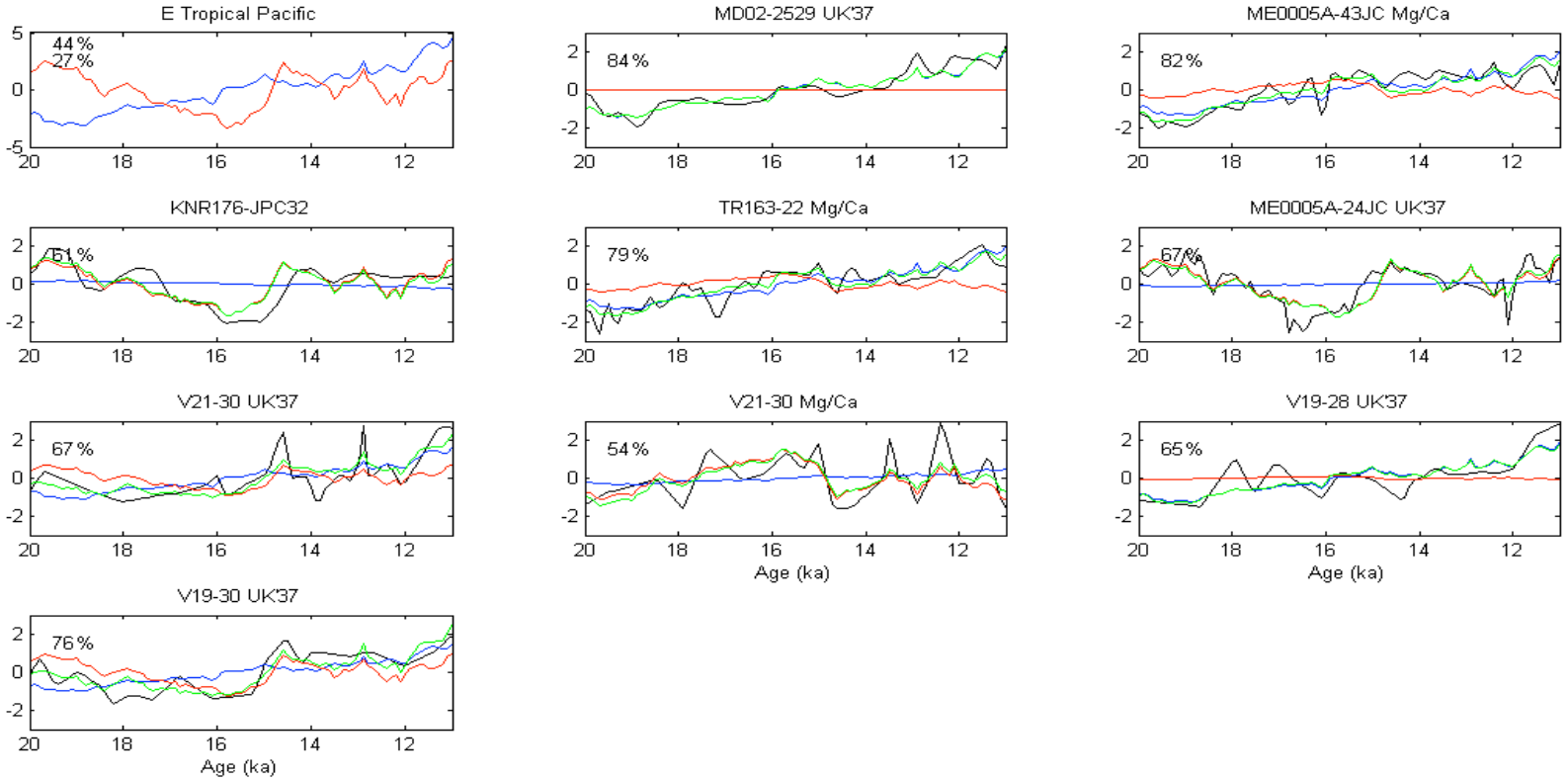

Figure S8 (continued).

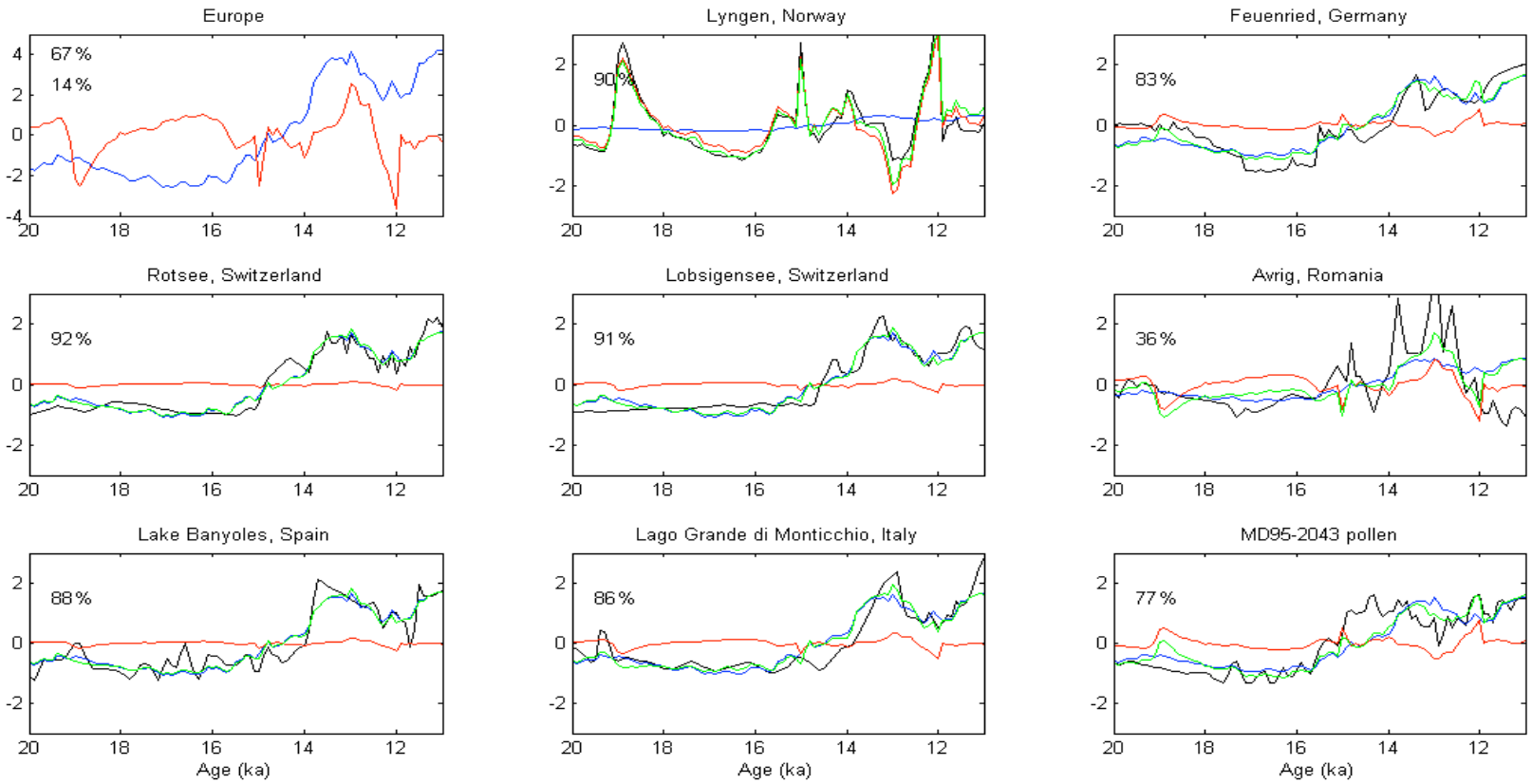

Figure S8 (continued).

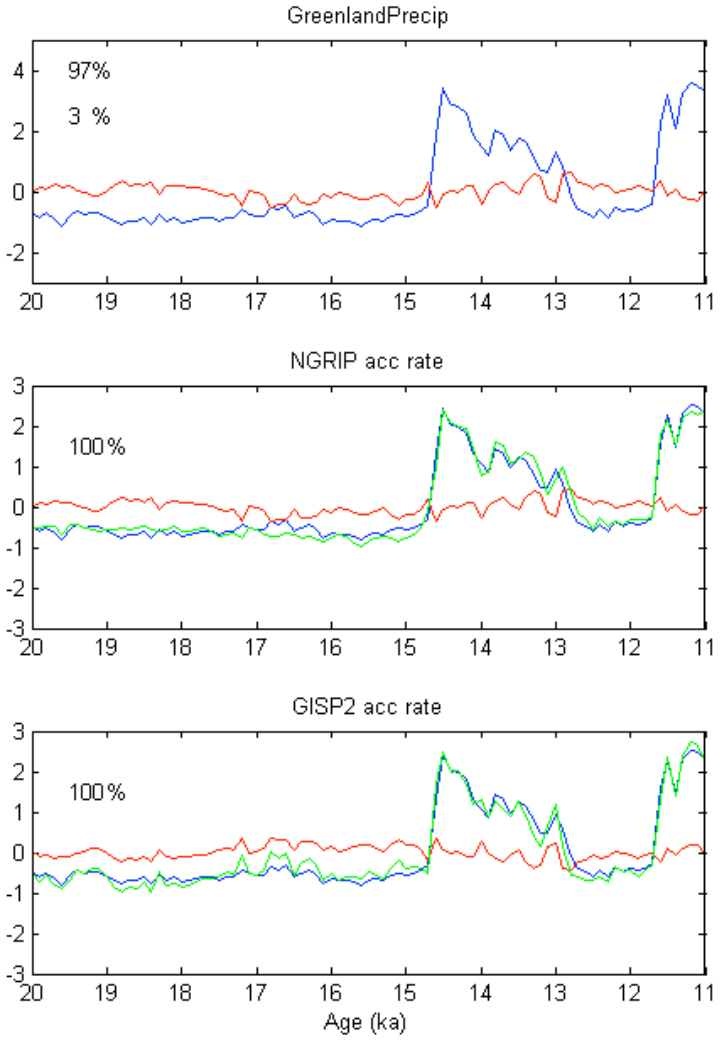

Figure S8 (continued).

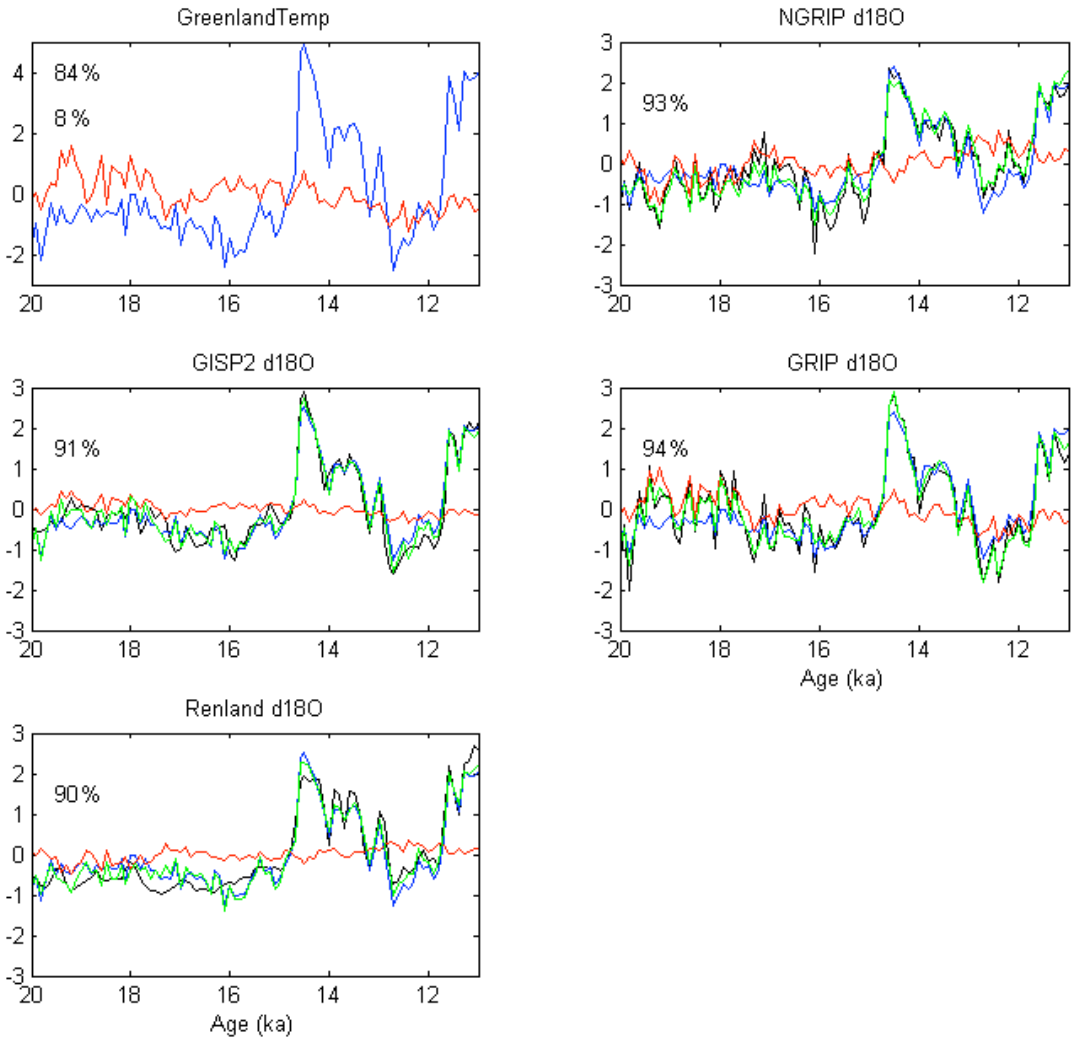

Figure S8 (continued).

Figure S8 (continued).

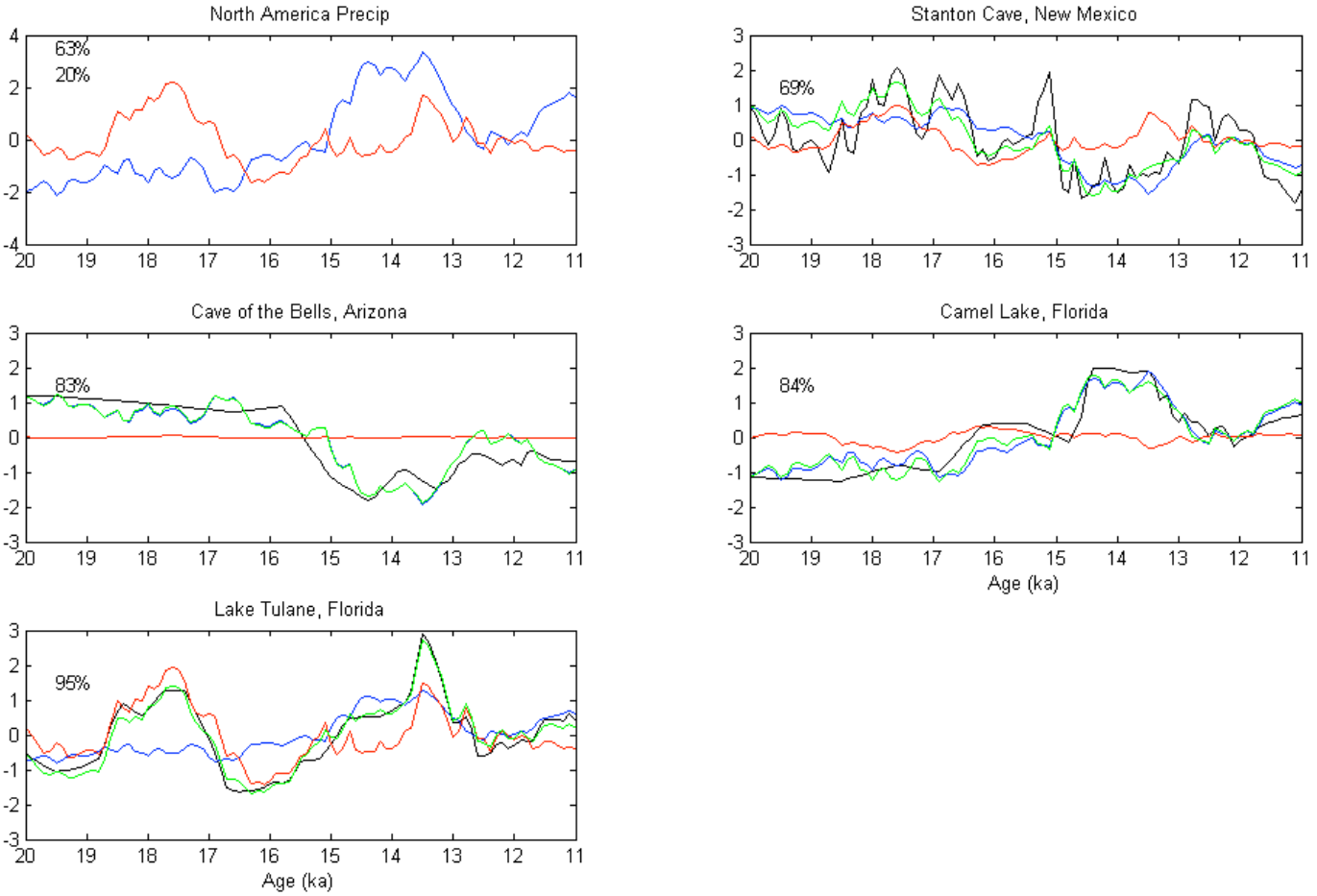

Figure S8 (continued).

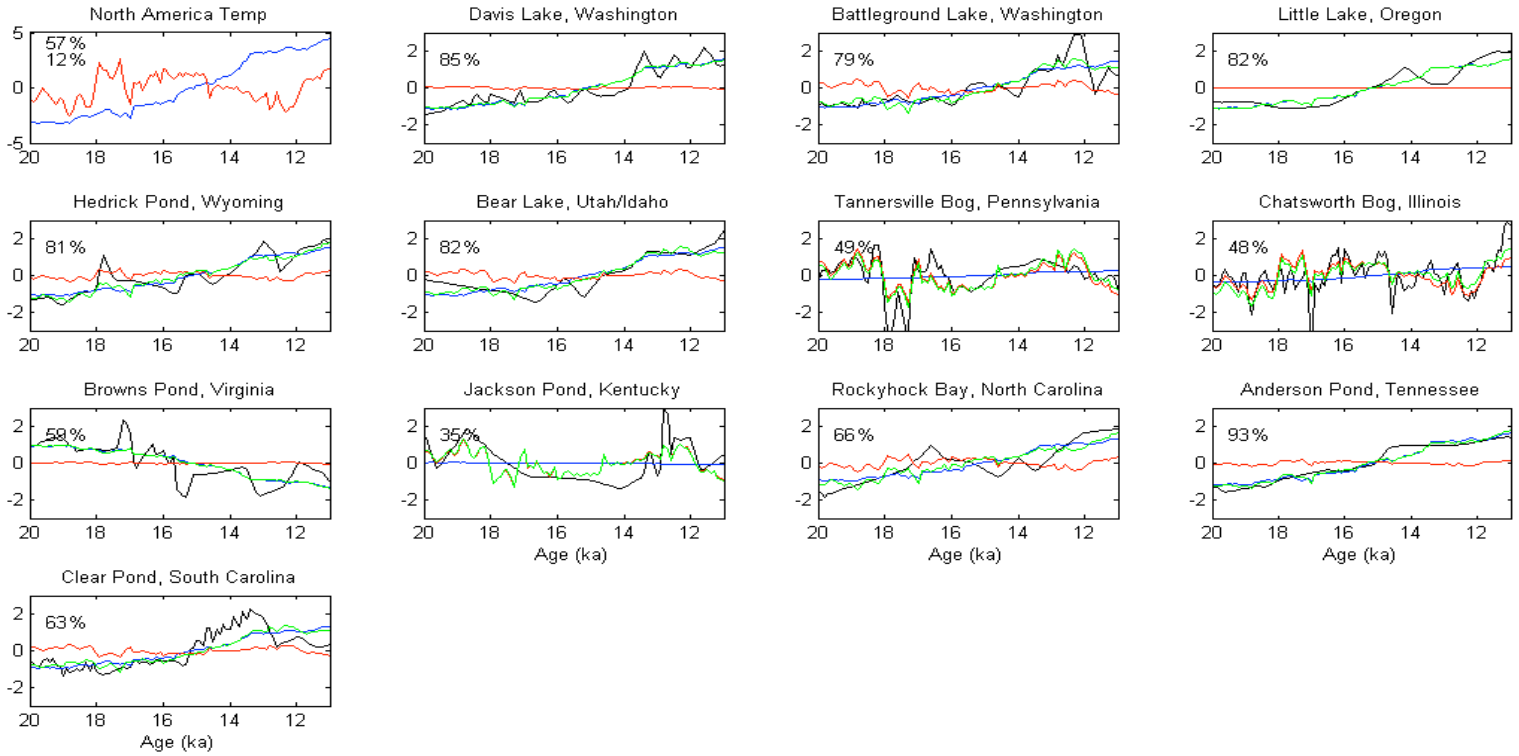

Figure S8 (continued).

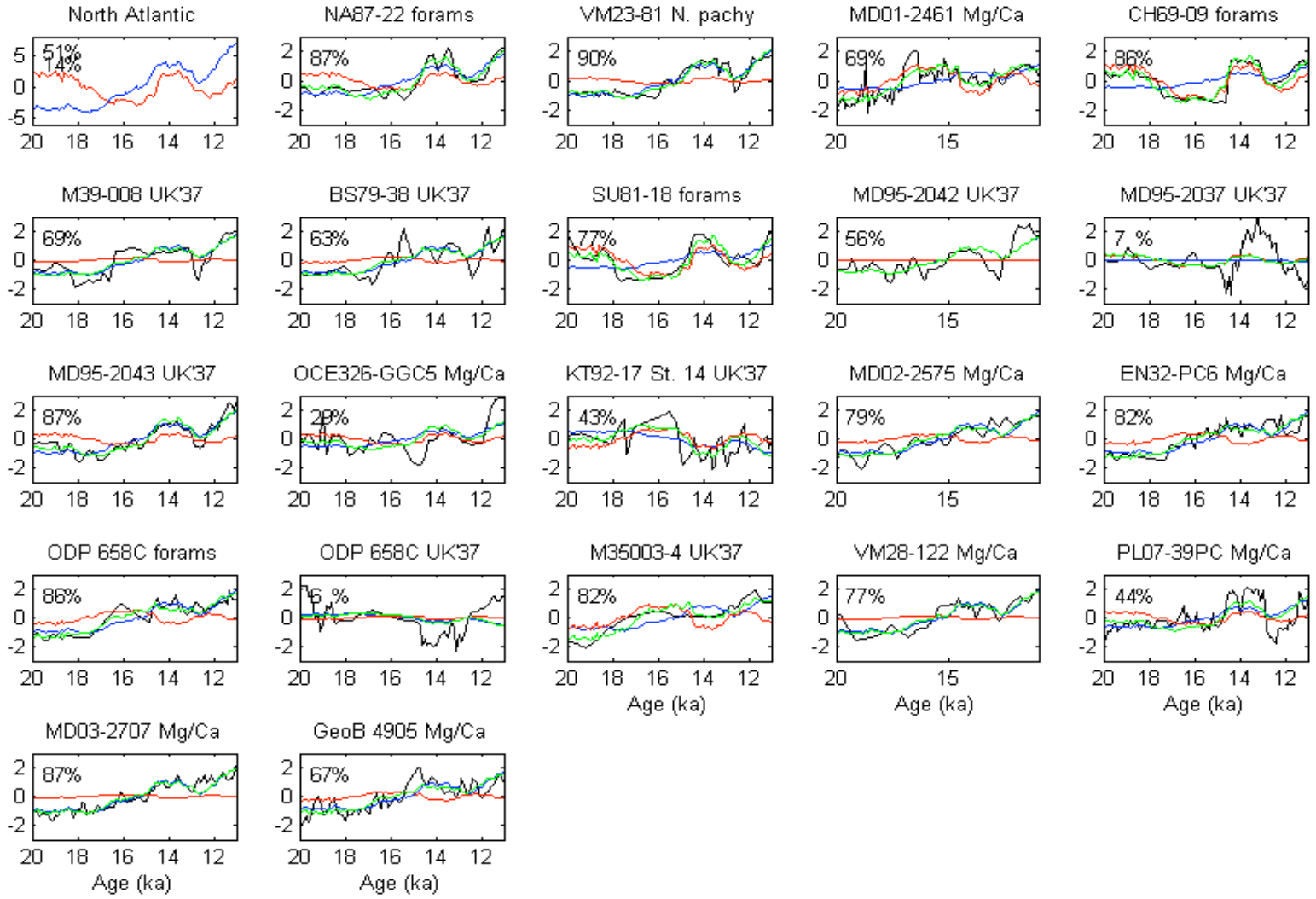

Figure S8 (continued).

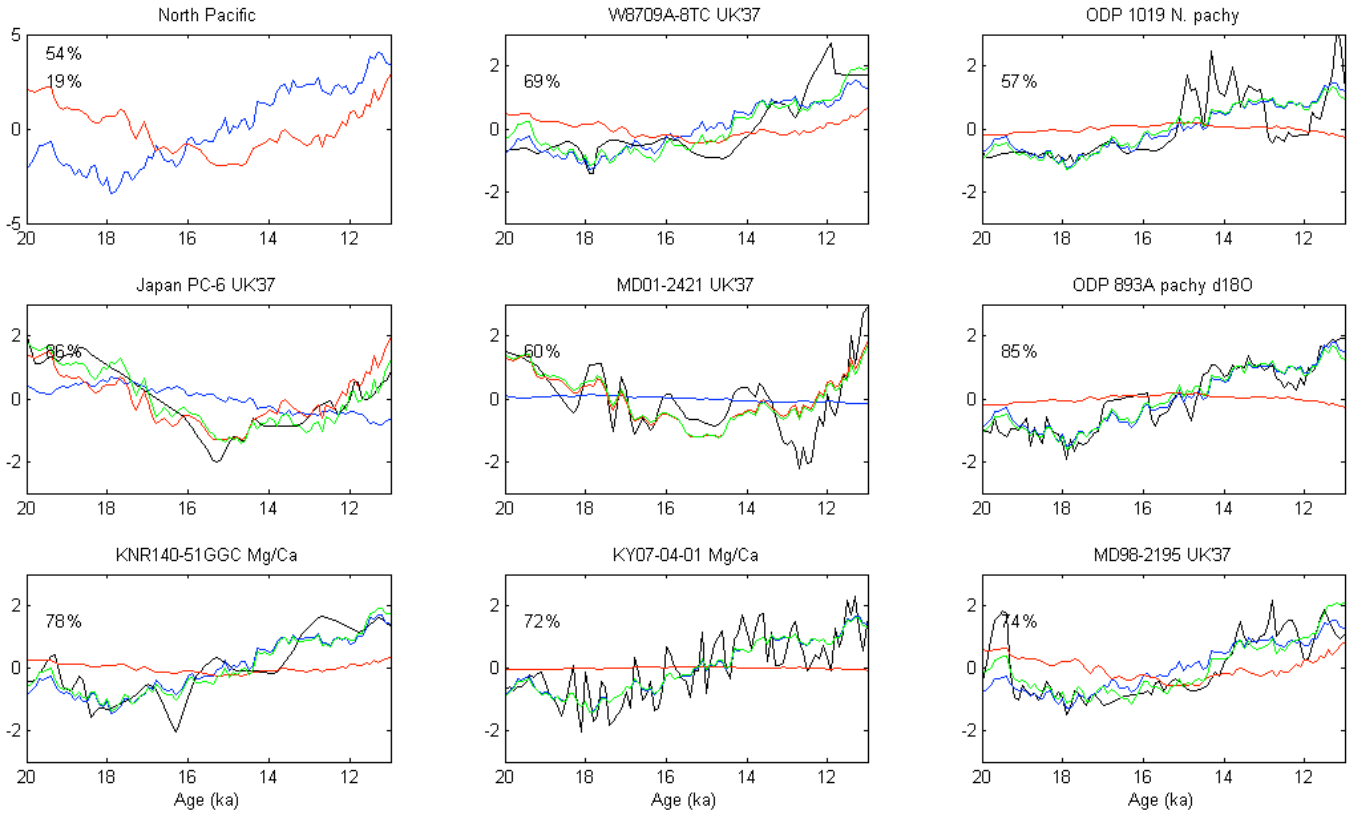

Figure S8 (continued).

Figure S8 (continued).

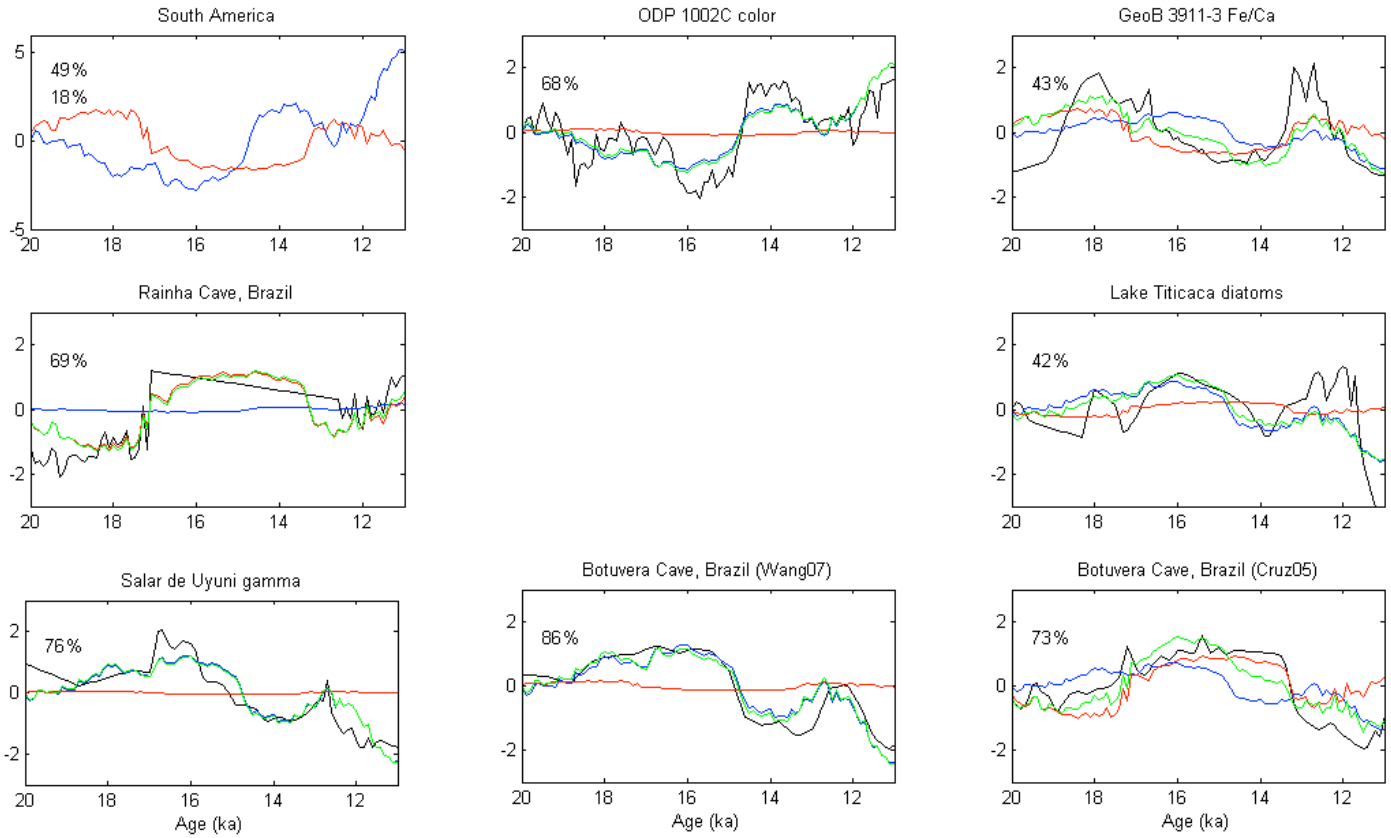

Figure S8 (continued).

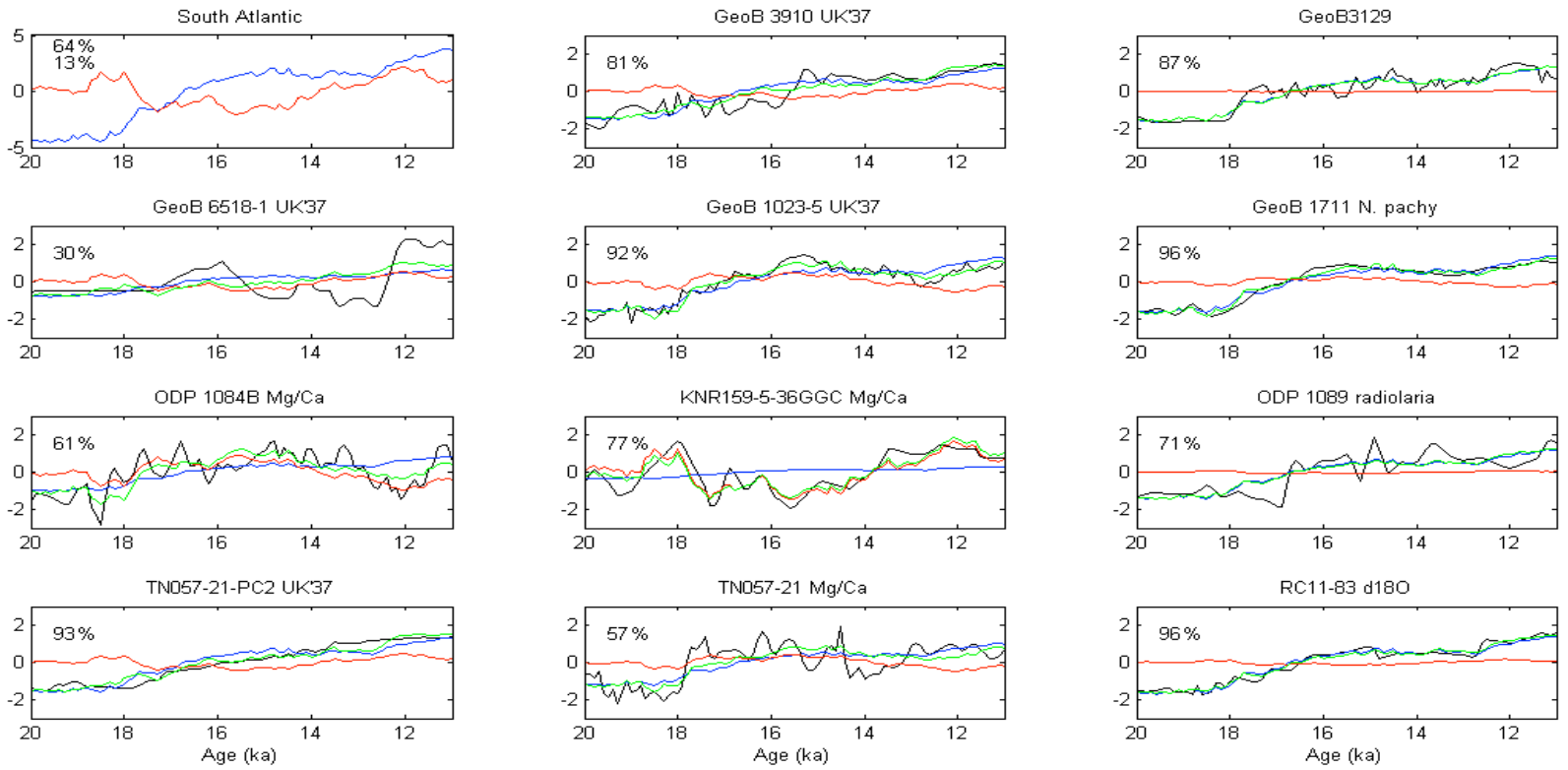

Figure S8 (continued).

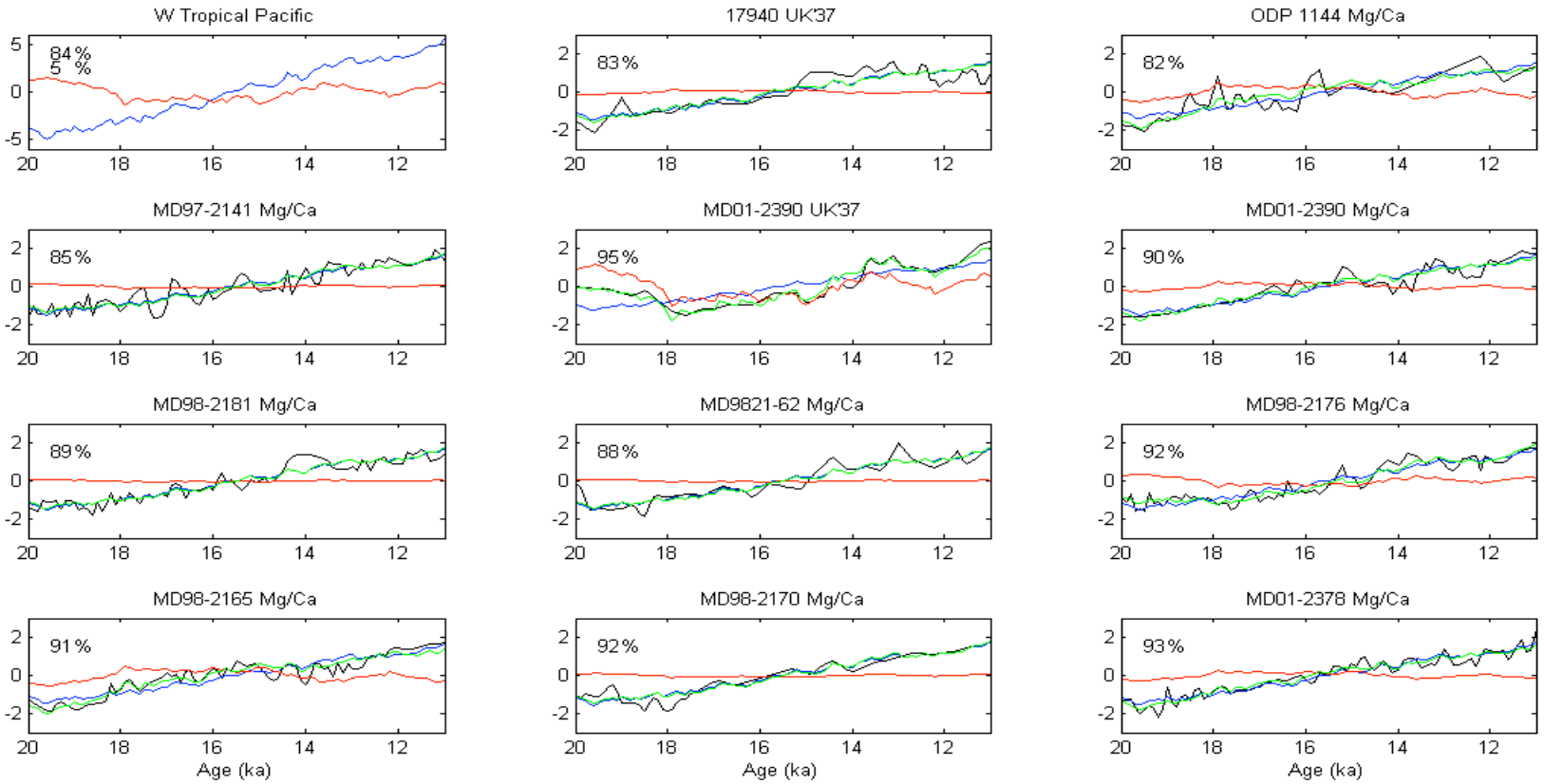

Figure S8 (continued).

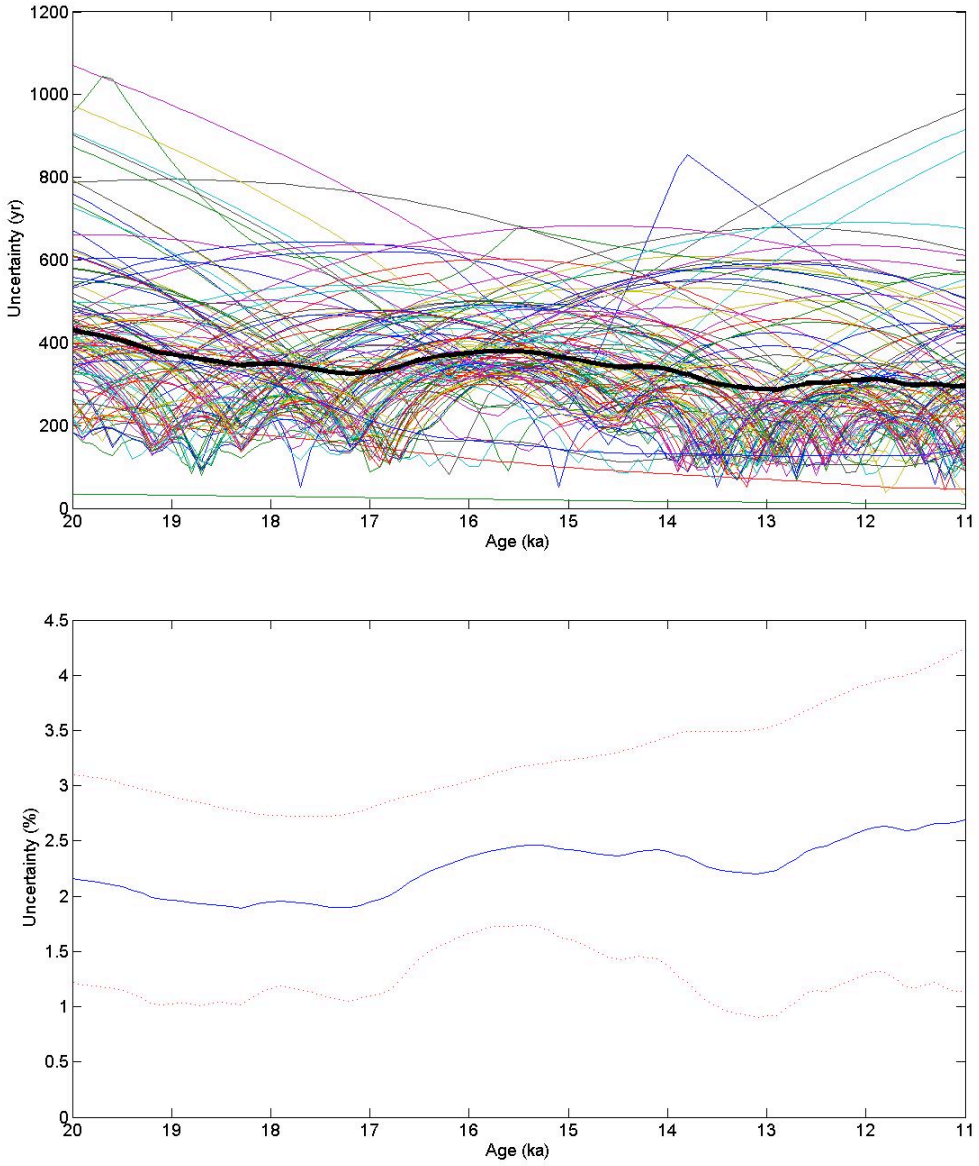

Figure S9: (**a**) Thin colored lines show the 1σ chronological uncertainty for individual records in the database, and the thick black line gives the average uncertainty. (**b**) The mean and standard deviation of the chronological uncertainties shown in (a), expressed as a percentage of age. The average uncertainty in the database is ~2%, which was therefore applied to the 37 records for which uncertainties could not be quantified.

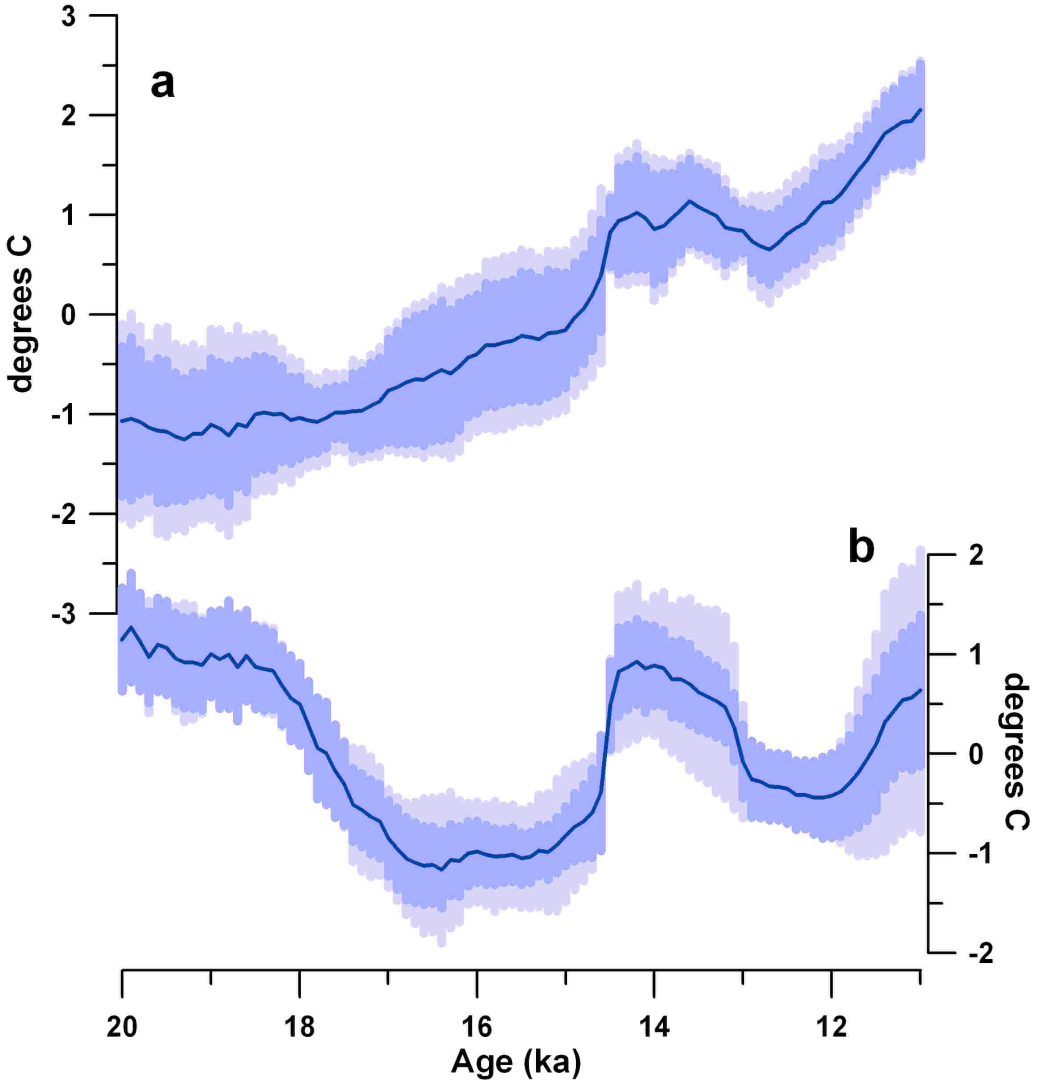

Figure S10: (**a**) PC1 and (**b**) PC2 for 69 deglacial SST records (blue lines). The standard deviation of 1000 Jackknifed PCs after randomly excluding 68% and 95% of the records are shown by the darker and lighter blue error bars.

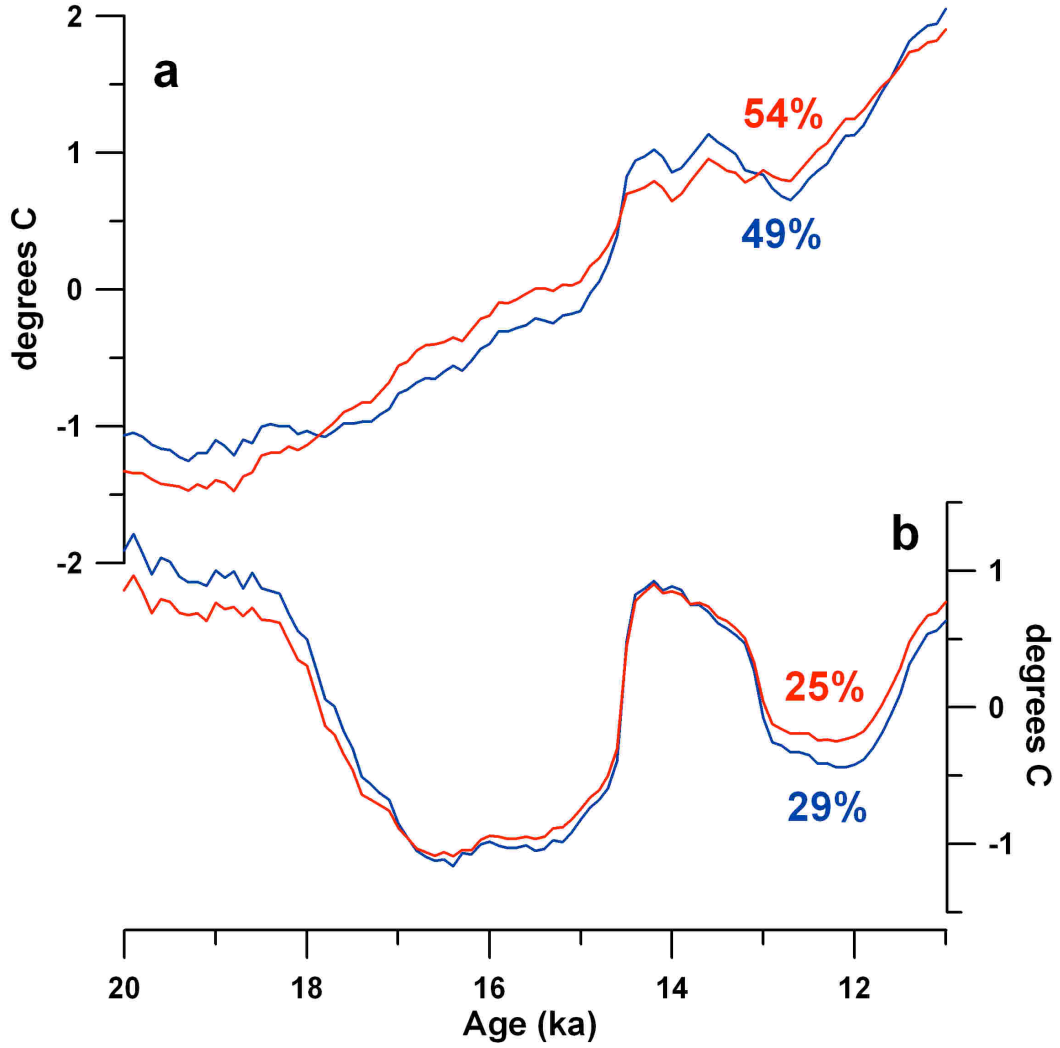

Figure S11: (**a**) PC1 and (**b**) PC2 for the 69 deglacial SST records (blue) and after including the Southern Hemisphere records twice (red). The percentage of variance explained by each is given.

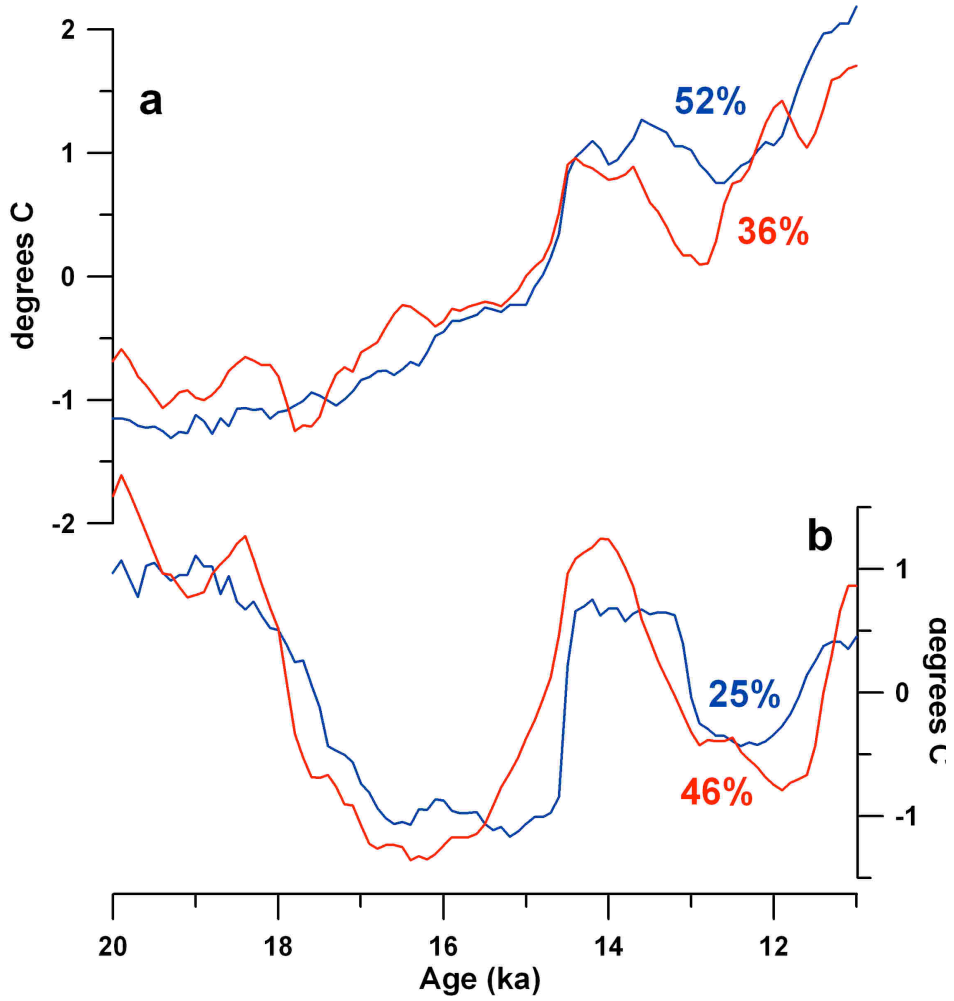

Figure S12: (**a**) PC1 for open-ocean sites (blue) and PC2 for upwelling sites (red). (**b**) PC2 for open-ocean sites (blue) and PC1 for upwelling sites (red). The percentage of variance explained by each is given.

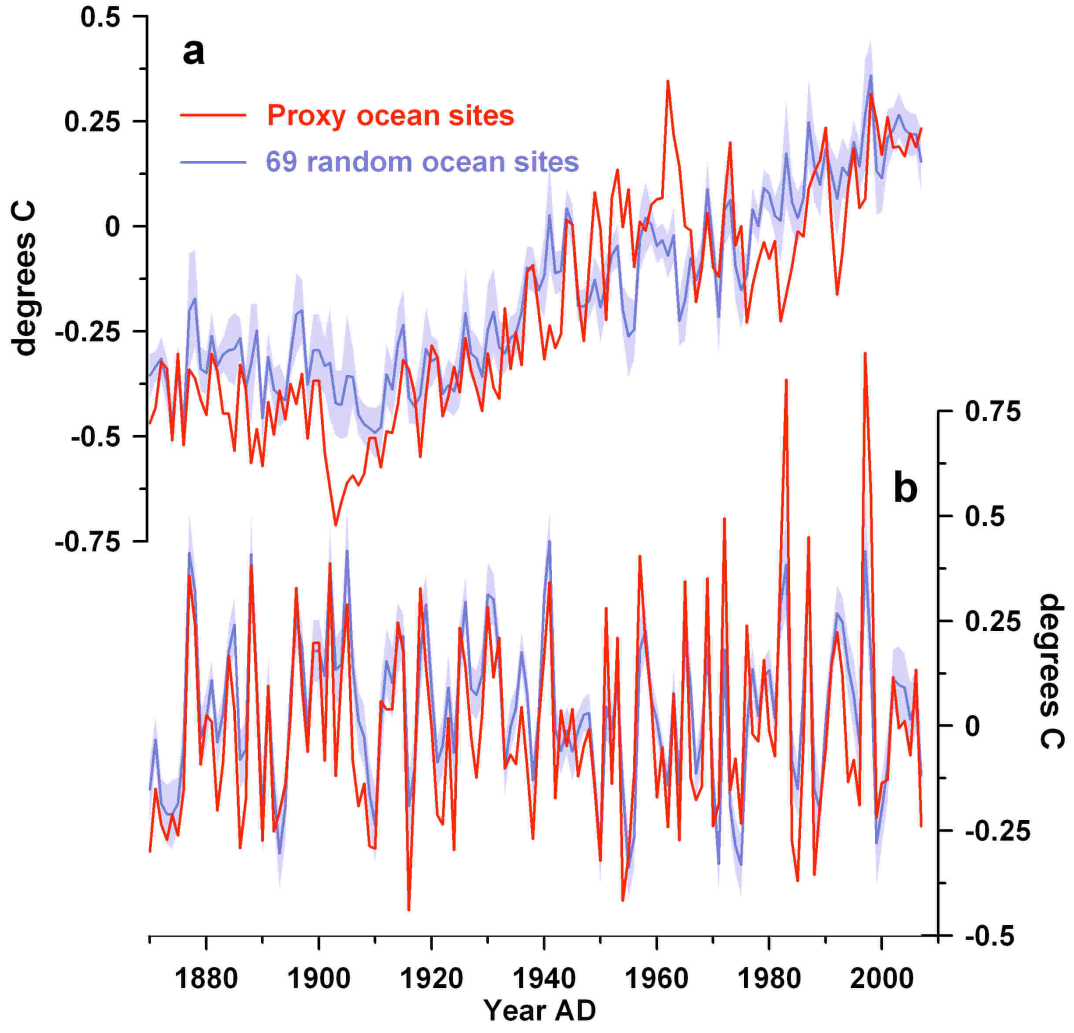

Figure S13: (**a**) PC1 and (**b**) PC2 for the HadSST2 dataset (blue lines). Blue error bars show the standard deviation of 1000 jackknifed PCs using 69 random locations for each iteration. Also shown are PC1 and PC2 for the specific locations of the 69 deglacial SST records (red).

References

1. Jensen K (1935) Archaeological dating in the history of North Jutland's vegetation. *Acta Archaeologica* 5:185-214.
2. Iversen J (1954) The late-glacial flora of Denmark and its relationship to climate and soil. *Danmarks Geologische Undersogelse Series II* 75:1-175.
3. Rasmussen SO*, et al.* (2006) A new Greenland ice core chronology for the last glacial termination. *Journal of Geophysical Research-Atmospheres* 111(D6).
4. Mangerud J, Andersen ST, Berglund BE, & Donner JJ (1974) Quaternary stratigraphy of Norden, a proposal for terminology and classification. *Boreas* 3:109-128.
5. Björck S*, et al.* (1998) An event stratigraphy for the Last Termination in the North Atlantic region based on the Greenland ice-core record: a proposal by the INTIMATE group. *Journal of Quaternary Science* 13:283-292.
6. Mix AC, Ruddiman WF, & McIntyre A (1986) Late Quaternary paleoceanography of the tropical Atlantic, 1: spatial variability of annual mean sea-surface temperatures, 0-20,000 years B.P. *Paleoceanography* 1:43-66.
7. Shakun JD & Carlson AE (2010) A global perspective on Last Glacial Maximum to Holocene climate change. *Quaternary Science Reviews* 29(15-16):1801-1816.
8. Clark PU, Pisias NG, Stocker TF, & Weaver AJ (2002) The role of the thermohaline circulation in abrupt climate change. *Nature* 415:863-869.
9. Stouffer RJ*, et al.* (2006) Investigating the causes of the response of the thermohaline circulation to past and future climate changes. (Translated from English) *Journal of Climate* 19(8):1365-1387 (in English).
10. Weaver AJ, Saenko O, Clark PU, & Mitrovica JX (2003) Meltwater pulse 1A from Antarctica as a trigger of the Bølling-Allerød warm interval. *Science* 299:1709-1713.
11. Stouffer RJ, Seidov D, & Haupt BJ (2007) Climate response to external sources of freshwater: North Atlantic versus the Southern Ocean. *Journal of Climate* 20(3):436-448.
12. Kageyama M, Paul A, Roche DM, & Van Meerbeeck CJ (2010) Modelling glacial climatic millennial-scale variability related to changes in the Atlantic meridional overturning circulation: a review. *Quaternary Science Reviews* 29(21-22):2931-2956.
13. Otto-Bliesner BL & Brady EC (2010) The sensitivity of the climate response to the magnitude and location of freshwater forcing: last glacial maximum experiments. *Quaternary Science Reviews* 29(1-2):56-73.
14. Spence JP, Eby M, & Weaver AJ (2008) The sensitivity of the Atlantic meridional overturning circulation to freshwater forcing at eddy-permitting resolutions. *Journal of Climate* 21(11):2697-2710.
15. Wunsch C (2010) Towards understanding the Paleocean. *Quaternary Science Reviews* 29(17-18):1960-1967.
16. Clark PU*, et al.* (2009) The Last Glacial Maximum. *Science* 325:710-714.
17. Carlson AE & Clark PU (submitted) Sources of sea-level rise and freshwater discharge during the last deglaciation. *Reviews of Geophysics*.
18. Yokoyama Y, Lambeck K, De Deckker P, Johnston P, & Fifield LK (2000) Timing of the Last Glacial Maximum from observed sea-level minima. (Translated from English) *Nature* 406(6797):713-716 (in English).
19. Clark PU, McCabe AM, Mix AC, & Weaver AJ (2004) Rapid rise of sea level 19,000 years ago and its global implications. *Science* 304(5674):1141-1144.

20. Materials and methods are available as supporting material on Science Online.
21. Clark PU*, et al.* (2009) The Last Glacial Maximum. *Science* 325(5941):710-714.
22. Dyke AS (2004) An outline of North American deglaciation with emphasis on central and northern Canada. *Quaternary Glaciations: Extent and Chronology*, eds Ehlers J & Gibbard PL (Elsevier, Amsterdam), Vol 2b, pp 373-424.
23. Flower BP, Hastings DW, Hill HW, & Quinn TM (2004) Phasing of deglacial warming and laurentide ice sheet meltwater in the Gulf of Mexico. *Geology* 32(7):597-600.
24. Rinterknecht VR*, et al.* (2006) The last deglaciation of the southeastern sector of the Scandinavian Ice Sheet. *Science* 311(5766):1449-1452.
25. Hemming SR (2004) Heinrich events: Massive late Pleistocene detritus layers of the North Atlantic and their global climate imprint. *Reviews of Geophysics* 42(1).
26. Keigwin LD, Jones GA, Lehman SJ, & Boyle EA (1991) Deglacial meltwater discharge, North Atlantic deep circulation, and abrupt climate change. *Journal of Geophysical Research* 96:16811-16826.
27. Fairbanks RG, Charles CD, & Wright JD (1992) Origin of global meltwater pulses. *Radiocarbon after four decades*, ed Taylor REea (Springer-Verlag), pp 473-500.
28. Aharon P (2006) Entrainment of meltwaters in hyperpycnal flows during deglaciation superfloods in the Gulf of Mexico. *Earth and Planetary Science Letters* 241(1-2):260-270.
29. Carlson AE, Clark PU, & Hostetler SW (2009) Comment: Radiocarbon deglaciation chronology of the Thunder Bay, Ontario area and implications for ice sheet retreat patterns. *Quaternary Science Reviews* 28(23-24):2546-2547.
30. Roche DM, Renssen H, Weber SL, & Goosse H (2007) Could meltwater pulses have been sneaked unnoticed into the deep ocean during the last glacial? *Geophysical Research Letters* 34(24).
31. McManus JF, Francois R, Gherardi J-M, Keigwin LD, & Brown-Leger S (2004) Collapse and rapid resumption of Atlantic meridional circulation linked to deglacial climate changes. *Nature* 428:834-837.
32. Mackintosh A*, et al.* (2011) Retreat of the East Antarctic ice sheet during the last glacial termination. *Nature Geoscience* 4:195-202.
33. Clark PU, Mitrovica JX, Milne GA, & Tamisiea ME (2002) Sea-level fingerprinting as a direct test for the source of global meltwater pulse IA. *Science* 295:2438-2441.
34. Bassett SE, Milne GA, Mitrovica JX, & Clark PU (2005) Ice sheet and solid earth influences on far-field sea-level histories. *Science* 309(5736):925-928.
35. Bassett SE, Milne GA, Bentley MJ, & Huybrechts P (2007) Modelling Antarctic sea-level data to explore the possibility of a dominant Antarctic contribution to meltwater pulse IA. (Translated from English) *Quaternary Science Reviews* 26(17-18):2113-2127 (in English).
36. Fairbanks RG (1989) A 17,000-year glacio-eustatic sea level record: influence of glacial melting rates on the Younger Dryas event and deep-ocean circulation. *Nature* 342:637-642.
37. Bard E, Hamelin B, & Delanghe-Sabatier D (2010) Deglacial meltwater pulse 1B and Younger Dryas sea levels revisited with boreholes at Tahiti. *Science* 327(5970):1235-1237.
38. Johnson RG & McClure BT (1976) A model for northern hemisphere continental ice sheet variation. *Quaternary Research* 6:325-353.

39. Rooth C (1982) Hydrology and ocean circulation. *Progress in Oceanography* 11:131-149.
40. Licciardi JM, Teller JT, & Clark PU (1999) Freshwater routing by the Laurentide Ice Sheet during the last deglaciation. *Mechanisms of Global Climate Change at Millennial Time Scales*, eds Clark PU, Webb RS, & Keigwin LD (American Geophysical Union, Washington, D.C.), Vol Geophysical Monograph 112, pp 177-201.
41. Fisher TG (2003) Chronology of glacial Lake Agassiz meltwater routed to the Gulf of Mexico. *Quaternary Research* 59(2):271-276.
42. Broecker WS*, et al.* (1989) Routing of meltwater from the Laurentide ice sheet during the Younger Dryas cold episode. *Nature* 341(6240):318-321.
43. Keigwin LD & Jones GA (1995) The marine record of deglaciation from the continental margin off Nova Scotia. *Paleoceanography* 10:973-985.
44. deVernal A, HillaireMarcel C, & Bilodeau G (1996) Reduced meltwater outflow from the laurentide ice margin during the Younger Dryas. *Nature* 381(6585):774-777.
45. Teller JT, Leverington DW, & Mann JD (2002) Freshwater outbursts to the oceans from glacial Lake Agassiz and their role in climate change during the last deglaciation. *Quaternary Science Reviews* 21(8-9):879-887.
46. Tarasov L & Peltier WR (2005) Arctic freshwater forcing of the Younger Dryas cold reversal. *Nature* 435(7042):662-665.
47. Teller JT, Boyd M, Yang ZR, Kor PSG, & Fard AM (2005) Alternative routing of Lake Agassiz overflow during the Younger Dryas: new dates, paleotopography, and a re-evaluation. *Quaternary Science Reviews* 24(16-17):1890-1905.
48. Murton JB, Bateman MD, Dallimore SR, Teller JT, & Yang ZR (2010) Identification of Younger Dryas outburst flood path from Lake Agassiz to the Arctic Ocean. *Nature* 464(7289):740-743.
49. Lowell TV*, et al.* (2009) Radiocarbon deglaciation chronology of the Thunder Bay, Ontario area and implications for ice sheet retreat patterns. *Quaternary Science Reviews* 28(17-18):1597-1607.
50. Carlson AE*, et al.* (2007) Geochemical proxies of North American freshwater routing during the Younger Dryas cold event. *Proceedings of the National Academy of Sciences of the United States of America* 104(16):6556-6561.
51. Dale B (1996) Dinoflagellate cyst ecology: modeling and geological applications. *Palynology: Principles and Applications*, eds Jansonius J & McGregor DG (AASP Foundation), Vol 3, pp 1249-1275.
52. Telford RJ (2006) Limitations of dinoflagellate cyst transfer functions. *Quaternary Science Reviews* 25(13-14):1375-1382.
53. Colman SM, Keigwin LD, & Forester RM (1994) Two episodes of meltwater influx from glacial Lake Agassiz into the Lake Michigan basin and their climatic contrasts. *Geology* 22(6):547-550.
54. Meissner KJ & Clark PU (2006) Impact of floods versus routing events on the thermohaline circulation. *Geophysical Research Letters* 33(15).
55. Clarke GKC, Bush ABG, & Bush JWM (2009) Freshwater discharge, sediment transport, and modeled climate impacts of the final drainage of glacial Lake Agassiz. *Journal of Climate* 22:2161-2180.
56. Carlson AE & Clark PU (2008) Rapid climate change and Arctic Ocean freshening: Comment. *Geology* 36:e137.

57. Reimer PJ*, et al.* (2009) Intcal09 and Marine09 radiocarbon age calibration curves, 0-50,000 years cal BP. *Radiocarbon* 51(4):1111-1150.
58. Huybers P & Wunsch C (2004) A depth-derived Pleistocene age model: Uncertainty estimates, sedimentation variability, and nonlinear climate change. *Paleoceanography* 19(1).
59. Lemieux-Dudon B*, et al.* (2010) Consistent dating for Antarctic and Greenland ice cores. *Quaternary Science Reviews* 29(1-2):8-20.
60. Rayner NA*, et al.* (2006) Improved analyses of changes and uncertainties in sea surface temperature measured in situ sice the mid-nineteenth century: The HadSST2 dataset. *Journal of Climate* 19(3):446-469.
61. Gherardi JM*, et al.* (2009) Glacial-interglacial circulation changes inferred from Pa-231/Th-230 sedimentary record in the North Atlantic region. *Paleoceanography* 24.
62. Negre C*, et al.* (2010) Reversed flow of Atlantic deep water during the Last Glacial Maximum. *Nature* 468(7320):84-89.